NASA Technical Memorandum 84523

# Operational Evaluation of a Propeller Test Stand in the Quiet Flow Facility at Langley Research Center

P. J. W. Block
*Langley Research Center*
*Hampton, Virginia*

National Aeronautics
and Space Administration

**Scientific and Technical
Information Branch**

1982

## INTRODUCTION

The study of propeller noise is motivated by the need for both quiet and efficient propellers. Although analytical tools are currently available for predicting the performance and noise of propellers (refs. 1 to 4), their merit and range of applicability must be determined by careful experiments. High-quality noise data uncontaminated by facility background noise and reflections must be obtained in an anechoic flow environment. The operational evaluation of a propeller test stand (PTS) in an open-jet flow environment is the subject of this study.

Presented in this report are the results of operational proof tests of the PTS in the quiet flow facility (QFF) of the Langley Aircraft Noise Reduction Laboratory (ANRL). The PTS is an experimental test-bed for acoustic propeller research in the quiet flow environment of the QFF. The purpose of these proof tests was to validate thrust and torque predictions, to examine the repeatability of measurements on the PTS, and to determine the effect of applying artificial roughness to the propeller blades. Since a thrusting propeller causes an open jet to contract, the potential-flow core was surveyed to examine the magnitude of the contraction. These measurements are compared with predicted values. The predictions are used to determine operational limitations for testing a given propeller design in the QFF.

Aerodynamic performance is predicted from a model based on blade element theory, momentum theory, and the Goldstein-Lock tip relief correction (refs. 5 and 6). The method requires that the aerodynamic characteristics of each blade station, or element, be provided in order to predict the thrust and power coefficients ($C_T$ and $C_p$) of the propeller. This method is described in appendix A. The basis for predicting the potential core radius is simple actuator disk theory, described in appendix B.

In this report, the PTS hardware and test setup in the QFF are described, and then the flow survey and aerodynamic results are presented. An acoustic experiment was not performed since the purpose of this study was the electrical and mechanical evaluation of a new piece of experimental equipment in an open-jet flow and the evaluation of propeller performance prediction codes.

## SYMBOLS

Dimensional quantities are presented in both the International System of Units (SI) and U.S. Customary Units. Measurements and calculations were made in SI Units.

$A_{body}$ area of the PTS centerbody

$A_{disk}$ area of propeller disk

$A_j$ area of the jet exit

$A_s$ upstream area of streamtube cross section that contracts to the propeller tips at the disk plane

$A_T$ total thrusting area, $A_{disk} - A_{body}$

| | |
|---|---|
| $aV_a$ | axial component of induced velocity (see the sketch in appendix A) |
| $a'r\Omega$ | azimuthal component of induced velocity (see the sketch in appendix A) |
| B | number of propeller blades |
| b | chord of propeller blade element |
| $C_P$ | power coefficient, $P/\rho n^3 d_p^5$ |
| $C_T$ | thrust coefficient, $T/\rho n^2 d_p^4$ |
| $c_d$ | two-dimensional drag coefficient of propeller blade element (see appendix A) |
| $c_\ell$ | two-dimensional lift coefficient of propeller blade element (see appendix A) |
| d | drag of airfoil section |
| $d_{body}$ | diameter of PTS centerbody |
| $d_j$ | jet diameter |
| $d_p$ | propeller diameter |
| F | tip correction factor |
| f | factor in Prandtl-Betz correction |
| J | advance ratio, $U_j/nd_p$ |
| $\ell$ | lift of airfoil section |
| n | number of revolutions per second |
| P | propeller power |
| p | absolute pressure |
| Q | propeller torque |
| q | stagnation pressure minus static pressure, $\rho U_j^2/2$ |
| R | propeller radius |
| r | radial position of an elemental airfoil section of the propeller |
| $r_o$ | potential-flow core radius at the propeller disk plane |
| $r_s$ | upstream radius of the propeller streamtube |
| $\Delta r$ | radial distance between the propeller tips and the shear layer of the potential-flow core of the jet |

| | |
|---|---|
| $T$ | propeller thrust |
| $U$ | mean flow velocity |
| $U_j$ | jet-exit velocity |
| $V$ | velocity across propeller airfoil section (see appendix A) |
| $V_a$ | axial flow velocity (see appendix A) |
| $v$ | axial flow velocity caused by propeller momentum disk (see appendix B) |
| $z$ | distance downstream of jet exit plane |
| $\alpha$ | actual aerodynamic angle of attack of the propeller blade section (see appendix A) |
| $\beta$ | geometric pitch angle of the propeller blade section (see appendix A) |
| $\lambda$ | $J/\pi nd$ |
| $\rho$ | air density |
| $\sigma$ | solidity, $bB/2\pi r$ |
| $\phi$ | effective pitch angle of the propeller blade section (see appendix A) |
| $\Omega r$ | angular velocity (see the sketch in appendix A) |
| $\omega r/2$ | induced angular velocity (see the sketch in appendix A) |

Subscripts:

| | |
|---|---|
| amb | ambient value |
| max | maximum |
| meas | measured value |
| pred | predicted |

Abbreviations:

| | |
|---|---|
| ANRL | Aircraft Noise Reduction Laboratory |
| PTS | propeller test stand |
| QFF | quiet flow facility |
| rpm | revolutions per minute |

## DESCRIPTION OF MODEL AND APPARATUS

### Propeller Test Stand

A schematic of the PTS is shown in figure 1. A cylinder, 1.93 m (76 in.) long and 0.229 m (9 in.) in diameter, houses a 50-hp water-cooled electric motor, which is controlled by a solid-state variable-frequency motor controller (400 cps max, 60 kV-A max power). The motor used in this test was limited to 40.7 N-m (30 ft-lb) of torque, and the maximum speed was 8000 rpm. The motor, propeller, torque motor, and all rotating parts are supported by a thrust load cell which is aft of the motor and grounded to the case. With this load path, the drag of the entire centerbody nacelle was not registered on the load cell. Torque is measured by an in-line rotating-shaft torque sensor, which is isolated by two decouplers.

It should be pointed out that a more powerful motor can be employed as long as its physical size does not exceed 0.159 m (6.25 in.) in diameter and 0.457 m (18 in.) in length.

### Propeller

For the PTS evaluation, a two-bladed propeller design for use on an rpv (remotely piloted vehicle) was used and is shown in figure 2. It has ARA airfoil sections (7 percent at the tip, 9 percent at the root) and is 0.686 m (27 in.) in diameter. This propeller was designed for a speed range typical of that available in the ANRL QFF. Geometric pitch angles of 5° and 17° were set at 0.85 of the blade radius.

The propeller was first tested with smooth (polished) surfaces. Artificial roughness was applied to the suction surfaces and then to the pressure surfaces to examine the effect on propeller performance. The roughness was a nonstandard grit with the largest size approximating no. 60. It was applied in a band, 2.5 mm (1/10 in.) wide, 2.5 mm (1/10 in.) downstream of the leading edges.

### Quiet Flow Facility

The experimental setup in the QFF is shown in figure 3. No attempt was made to perserve the anechoic characteristics of the room, since no acoustic measurements were made during this test. The 1.22-m (4-ft) diameter circular nozzle currently has a maximum velocity of 36.6 m/s (120 ft/s), that is, Mach 0.11. It exhausts vertically into an anechoic room of dimensions 6.1 × 9.1 × 7.0 m high (20 × 30 × 23 ft high) between the wedge tips. Figure 4 is a sketch of the PTS in the QFF.

## TESTS AND CORRECTIONS

### Data Acquisition and Instrumentation

For each of the test conditions outlined in table I, the following measurements were made (see fig. 5 for complete instrumentation diagram). Outputs from four accelerometers placed on the centerbody were recorded for vibrational analyses. The thrust, torque, and rpm outputs were recorded on analog tape for vibrational analyses as well as stored in a computer for aerodynamic performance calculations. A microphone was placed in the chamber for diagnostic use. The air temperature in the noz-

zle plenum, the stagnation minus the static pressure 0.102 m (4 in.) inside the nozzle lip at the exit plane (q), and the ambient pressure ($p_{amb}$) in the anechoic room were measured and stored in the computer. Finally a pitot static tube was used in conjunction with a stepping motor to survey the potential core of the jet 0.15 m (6 in.) upstream and downstream of the propeller disk plane. These measurements provided the necessary data to evaluate the performance of the PTS, propeller, and QFF together and to validate predictions described in appendixes A and B.

## Data Reduction and Presentation

The data were obtained by increasing the rpm and then decreasing it through the desired range for the particular propeller blade pitch angle and forward velocity. The measured thrust and torque have been corrected for electrical and mechanical tares (which resulted from the body weight and the torque required to spin all but the blades). The thrust data were also corrected for the spinner drag, which was very small and varied almost linearly with velocity over the velocity range with a slope of 0.401 N/(m/s) (0.0275 lb/(ft/s)). This resulted in a drag of 14.7 N (3.3 lb) at the maximum velocity. The thrust and torque data have undergone two purges. One purge, described in appendix B, was necessitated by the potential core contraction at high thrust values. The other purge resulted from the thrust meter tare shifting continuously during the early phases of these tests. This purge is discussed in appendix C. The cause of the continuous shift was determined to be mechanical friction in the shaft bearing and load cell assembly and was rectifiable.

The air density $\rho$, which was calculated from the ambient pressure and the plenum temperature, was used to calculate the jet velocity as well as to nondimensionalize the thrust and power coefficients. All data presented are nondimensionalized. Aerodynamic data are presented in terms of the thrust and power coefficients versus propeller advance ratio ($J = U/nd_p$). Flow survey results are presented in terms of $U/U_j$ versus radial position in nozzle diameters.

Six conditions were repeated up to three times during the test program to examine the repeatability of the data. The rear shaft bearing temperature was recorded as an approximate indicator of the length of time that the PTS was operating. Generally the thrust and torque decrease slightly with increasing rear bearing temperature. However, in all cases the thrust- and torque-coefficient variation was less than 0.004. The size of the test-point symbols representing the performance data reflect the size of this uncertainty.

## FLOW SURVEY RESULTS

A primary concern when testing a propeller in an open-jet facility is the position of the jet shear layer with respect to the propeller blade tips. This problem is analyzed in appendix B, in which it is shown that the radial extent of the potential core is affected both by the centerbody, which expands the core, and by the propeller thrust, which contracts it. The effect of the centerbody has been included in the analysis.

## Effect of the Centerbody on the Potential Core

The effect of the centerbody alone on the radius of the potential core is shown in figure 6. The location of the knee (or outside edge) of the potential core $r_o$ was measured at a few positions downstream of the jet exit with and without the centerbody in the flow. It can be concluded from the figure that the centerbody had a small favorable effect on the extent of the potential core. This is expected and is shown in the analysis.

The velocity distribution in the potential core itself was measured 0.15 m (6 in.) upstream and downstream of the plane of the propeller disk without the propeller installed. The velocity profiles were nondimensionalized by the jet exit velocity, and the radial distance, by the jet diameter. Measurements were made at 19.5, 30, and 36.6 m/s (64, 98, and 120 ft/s). All velocity profiles collapsed well when normalized by $U_j$. The profiles upstream of the propeller disk location are given in figure 7, and those downstream, in figure 8. The radii of the centerbody and propeller are also indicated in the figures. These profiles are representative of the data taken at all velocities. The flow deceleration and acceleration around the body are clearly seen in the vicinity of the centerbody ($r/d_j \approx 0.1$), and the centerbody influence extends only out to $r/d_j = 0.19$. Also of note in figure 7 is that the potential core extends to about $r/d_j = 0.45$. This number is slightly larger than the value measured without the centerbody in the flow (see fig. 6).

## Effect of Propeller on the Potential Core

The jet was surveyed to locate the knee (or outside edge) of the potential core for comparison with the predictions given by equations (B5) and (B8). The measured profiles are given in figure 9 for a blade pitch angle of 5° and in figure 10 for a blade pitch angle of 17°. The solid line represents the profile measured 0.15 m (6 in.) upstream of the propeller disk plane, and the open symbols, the profile measured 0.15 m (6 in.) downstream of the propeller disk plane. The swirl component of the propeller slipstream velocity precludes exact measurement of the total velocity behind the propeller when using a nonaligning pitot static tube; however, the data of interest lie outside the slipstream and in the vicinity of the potential core knee. To obtain the knee location at the disk plane, the upstream and downstream knee locations are averaged.

Noted in figures 9 and 10 by an upward arrow is the average of the upstream and downstream locations of the potential core knee. Also noted in the figures is the predicted knee location ($r_o/d_j$ $_{pred}$). Table II summarizes the predicted values, the measured values, and the error in percent. The average difference between the measured and predicted location of the knee is less than 5 percent with the prediction consistently underestimating the actual (measured) value.

The largest errors (greater than 7 percent) in the predicted location of the potential core knee may have been caused by errors in the measured thrust, and thus in $C_T$, under particular conditions. In appendix B, bounds were established on propeller performance for which meaningful aerodynamic data can be obtained (see eq. (B12)). For the propeller used in this study, this criterion is $C_T/J^2 < 0.633$. If the three cases in table II for which $C_T/J^2 > 0.633$ are excluded, the average error is less than 3 percent. Thus the criterion of equation (B12) is a useful tool in determining possible limitations when testing a given propeller under various operating conditions in the QFF.

Thrust and torque data for runs where $C_T/J^2$ exceeded 0.633 were purged from the data base.

## AERODYNAMIC PERFORMANCE

### Reynolds Number

An examination of the effect of Reynolds number was attempted by placing grit at the 10 percent chord on the propeller blades. This grit is intended to create turbulent flow over the blades, and thus simulate the flow on full-scale propellers. Coplotted in figure 11 are the data for a blade pitch angle of 5° with surfaces smooth (polished), the suction surfaces roughened, and both the suction and the pressure surfaces roughened. Similar results for a blade pitch angle of 17° are given in figure 12 for two velocities. In general, the grit reduced the thrust (by about 11 percent at 17°). This dramatic reduction of $C_T$ is apparently due to a reduction in the section lift coefficient $c_\ell$ as shown by equation (A3). The addition of grit can erode the lift of an airfoil section in two ways. First, a typically low Reynolds number (500 000 based on the chord) coupled with a large grit size could result in a loss of lift and an increase in drag. Using a smaller grit size may eliminate this problem. Second, the boundary layer resulting from the grit may significantly change the effective airfoil shape and consequently alter its lift characteristics. It is conceivable that a thin turbulent boundary layer is not attainable at these Reynolds numbers, since a small grit is not sufficient to trip the boundary layer and a large grit adversely changes the effective airfoil shape or causes flow distortions (ref. 7). Thus a model-scale airfoil with a laminar boundary layer may more closely represent a full-scale airfoil with a turbulent boundary layer.

The torque also decreased with the addition of grit, because of diminished section lift, but the magnitude of the change was less than 5 percent at a blade pitch angle of 17°.

When both surfaces were roughened, little or no additional change was registered in the thrust, but the torque continued to decrease slightly.

### Comparison With Performance Predictions

The performance predicted from the method outlined in appendix A is plotted on figures 13 and 14 for blade pitch angles of 5° and 17°. In general, the predictions agreed well with the measured data. In all cases, the prediction agreed better with the smooth blade performance.

## EVALUATION OF RESULTS

The results of the flow survey and potential core "knee" prediction indicate a clear limitation (eq. (B12)) on the propeller conditions that can be tested on the PTS in the QFF. However, this limitation is not severe. Equation (B12) indicates that the upper bound on $C_T/J^2$ depends on the centerbody and jet-exit diameters as well as the propeller diameter. This upper bound $(C_T/J^2)_{max}$ is given as a function of propeller diameter for the PTS in the QFF in figure 15. As expected, smaller propellers can be operated at higher disk thrust loadings for a fixed advance ratio J. This allows sufficient potential core beyond the propeller tips to simulate free-

stream conditions. Also, smaller propeller diameters permit higher power loadings (horsepower/diameter$^2$) to be simulated. At present the maximum power for this test-bed is 50 hp (intermittent duty) at 8000 rpm, although this can be increased. On the other hand, decreasing the diameter reduces the maximum helical tip Mach number attainable (which is of importance in acoustic testing), since the maximum rotational speed attainable is 8000 rpm and jet-exit velocity is 36.6 m/s (120 ft/s). The maximum helical tip Mach number attainable with this test-bed as a function of propeller diameter is shown in figure 16. Two other considerations when testing a smaller diameter propeller are the Reynolds number and the ratio of propeller diameter to nacelle diameter.

At a nominal value of 7000 rpm for a moderately loaded propeller, the electric motor delivers up to 40 hp. With a 0.67-m (2.2-ft) diameter propeller (which allows tip Mach numbers of interest), a maximum power loading of 8.3 hp/ft$^2$ (to as high as 15 hp/ft$^2$ with a large motor) is obtained. Figure 17 indicates the class of aircraft whose propellers scale for testing on the PTS in the QFF. In this figure, a sample set of aircraft are simply classified by the maximum number of passengers they carry (ref. 8). The power plant and propeller together are described by the power loading. Roughly 1 hp/ft$^2$ is required per passenger. Thus with the present motor in the PTS, nominally 10-passenger aircraft and smaller can be scaled for an acoustic test in the QFF.

## CONCLUDING REMARKS

Operational proof tests have been performed on a propeller test stand (PTS) in the quiet flow facility of the Langley Aircraft Noise Reduction Laboratory. The PTS is an experimental test-bed for quiet propeller research. Flow surveys upstream and downstream of a propeller mounted on the PTS show that the propeller caused the potential flow core to contract by an amount that is well predicted by actuator disk theory. The same theory indicates that propeller operation at which meaningful aerodynamic data can be obtained is limited according to

$$\frac{C_T}{J^2} < \text{Constant}$$

where $C_T$ is thrust coefficient, $J$ is advance ratio, and the constant depends on the diameters of the propeller and jet. Another limitation is motor power; however, power can be increased as long as the motor can be housed in the PTS centerbody.

Thrust and torque coefficients measured on the PTS were repeatable within 0.004. The coefficients measured with smooth propeller blades (no grit) agreed well with predictions from a model based on blade element theory, momentum theory, and the Goldstein-Lock tip relief correction. The addition of grit to the blades decreased propeller thrust.

Langley Research Center
National Aeronautics and Space Administration
Hampton, VA 23665
August 10, 1982

## APPENDIX A

## PROPELLER PERFORMANCE PREDICTION

### Blade Element Theory

The lift and drag on an elemental two-dimensional airfoil section are written (ref. 1)

$$\delta \ell = \frac{1}{2} \rho V^2 c_\ell b \, \delta r \tag{A1}$$

$$\delta d = \frac{1}{2} \rho V^2 c_d b \, \delta r \tag{A2}$$

The lift and drag coefficients can be obtained in many ways; for the computation made herein, these coefficients were obtained from reference 2 for the ARA airfoil section.

From equations (A1) and (A2) and the propeller operating conditions, the forces in the axial direction (thrust) and the circumferential, or azimuthal, direction (torque) can be obtained for each element of the blade (see sketch):

$$\delta T = \frac{1}{2} \rho V^2 b \, \delta r \, B(c_\ell \cos \phi - c_d \sin \phi) \tag{A3}$$

$$\delta Q = \frac{1}{2} \rho V^2 br \, \delta r \, B(c_\ell \sin \phi + c_d \cos \phi) \tag{A4}$$

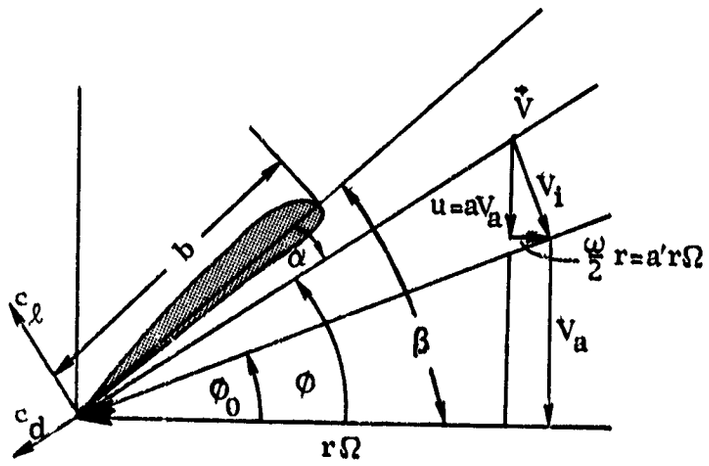


Here the unknowns are the actual inflow velocity $V$ and the angle $\phi$ of the flow into each station. The uncertainty comes from the induced velocity $V_i$ due to the wake vortex. At each station, the inflow velocity is written as a function of the

induced velocity ratio $a'$ or $a$. Thus the inflow to the propeller section can be written

$$V = V_a \frac{1 + a}{\sin \phi} = \Omega r \frac{1 - a'}{\cos \phi} \tag{A5}$$

When equation (A5) is substituted into equations (A3) and (A4), an expression is obtained for the thrust and torque in terms of the unknowns $a$ (or $a'$) and $\phi$:

$$\delta T = \frac{1}{2} \rho V_a^2 \frac{(1 + a)^2}{\sin^2 \phi} bB \, \delta r \left(c_\ell \cos \phi - c_d \sin \phi\right) \tag{A6}$$

$$\delta Q = \frac{1}{2} \rho V_a^2 \frac{(1 + a)^2}{\sin^2 \phi} bBr \, \delta r \left(c_\ell \sin \phi + c_d \cos \phi\right) \tag{A7}$$

Early attempts to obtain expressions for the unknowns came from axial and angular momentum statements which yield (ref. 1)

$$\frac{a}{1 + a} = \frac{\sigma}{4} \frac{c_\ell \cos \phi - c_d \sin \phi}{\sin^2 \phi} \tag{A8}$$

$$\frac{a'}{1 - a'} = \frac{\sigma}{4} \frac{c_\ell \sin \phi + c_d \cos \phi}{\sin \phi \cos \phi} \tag{A9}$$

The third relationship between $a$, $a'$, and $\phi$ comes from the geometric relationship

$$\tan \phi = \frac{V_a(1 + a)}{\Omega r(1 - a')} \tag{A10}$$

With an initial estimate of effective pitch angle $\phi_0$, equations (A8), (A9), and (A10) are solved iteratively for each blade section. The values for $a$ or $a'$ and $\phi$ are substituted into equations (A6) and (A7), and the results are summed over the blade radius to calculate the thrust and torque.

## Tip Relief Corrections

The above procedure for obtaining propeller performance is called blade element theory and has been used extensively for propeller design and analysis. Initially to account for the three-dimensional effect, aspect ratio corrections were made to $c_\ell$ and $c_d$. These corrections were later replaced by the tip relief correction, which originated (ref. 1) for fixed wing applications. This correction gave good results for small advance ratios or for a large number of blades. The correction was written

$$F = \frac{2}{\pi} \cos^{-1} f \tag{A11}$$

where

$$f = \frac{B}{2}\frac{R - r}{R}\sqrt{\frac{1 + \lambda^2}{\lambda}} \tag{A12}$$

With the correction, equations (A8) and (A9) take the form

$$\frac{a}{1 + a} = \frac{\sigma}{4F}\frac{c_l \cos\phi - c_d \sin\phi}{\sin^2\phi} \tag{A13}$$

$$\frac{a'}{1 - a'} = \frac{\sigma}{4F}\frac{c_l \sin\phi + c_d \cos\phi}{\sin\phi \cos\phi} \tag{A14}$$

Goldstein (ref. 5) obtained the exact solution (incompressible) for the downwash across the propeller span, and Lock (ref. 6) cast these results in a format convenient for use in blade element theory. The Goldstein-Lock correction has the form

$$F = \frac{K(\phi, r/R, B)}{\cos^2\phi} \tag{A15}$$

where $K(\phi, r/R, B)$ has been tabulated. The Goldstein-Lock correction is applicable in cases where the propeller is not heavily loaded and has a small number of blades. For the computations made herein, the Goldstein-Lock correction was used.

## Nonuniform Inflow

Typical propeller operation occurs in a radially nonuniform inflow environment. This can be taken into account by modifying $V_a$ by a factor representing the percent of the uniform stream that the propeller section is experiencing. The inflow to the propeller is modeled by a panel method computer program that calculates the flow around the spinner, shroud, and nacelle of the PTS. This correction has also been applied to the predictions contained herein.

## APPENDIX B

### PREDICTION OF POTENTIAL CORE KNEE POSITION

Actuator disk theory is used to develop a relationship for the extent of the potential core at the propeller disk plane. From actuator disk theory,

$$T = 2\rho A_T v(U_j + v) \tag{B1}$$

where $v$ is the velocity added by the propeller at the disk plane. Equation (B1) is solved for $v$ yielding

$$v = \frac{-U_j + \sqrt{U_j^2 + 2T/\rho A_T}}{2} \tag{B2}$$

With the radial and circumferential velocity components at the disk plane neglected, the mass continuity equation can be approximated by

$$A_s U_j = A_T(U_j + v) \tag{B3}$$

where $A_s$ is the area of the streamtube, which contracts to the area of the propeller at the disk plane as shown in the sketch:

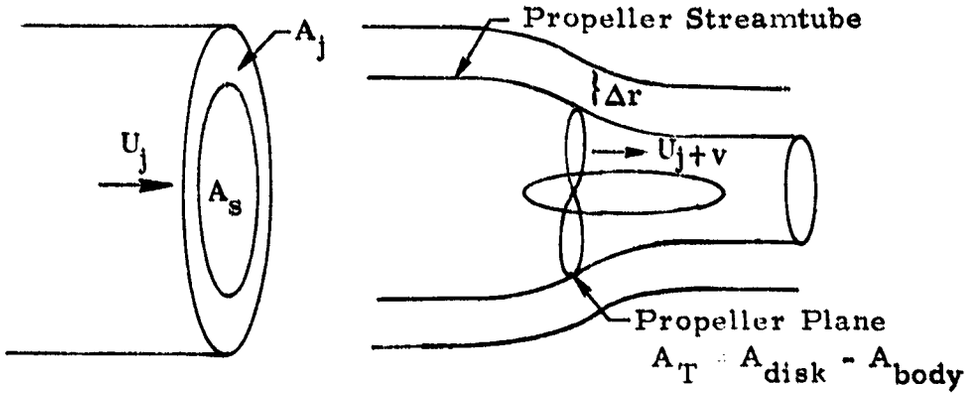


Substituting equation (B2) into (B3) yields

$$A_s U_j = A_T\left(\frac{U_j}{2} + \frac{1}{2}\sqrt{U_j^2 + \frac{2T}{\rho A_T}}\right) \tag{B4}$$

From the definitions

$$T = \rho n^2 d_p^4 C_T$$

and

$$J = \frac{U_j}{nd_p}$$



equation (B4) can be written

$$\frac{A_s}{A_T} = \frac{1}{2} + \frac{1}{2}\sqrt{1 + \frac{2d_p^2 C_T}{A_T J^2}} \tag{B5}$$

The ratio on the left side represents the contraction of the slipstream due to the addition of momentum at the disk plane. As $C_T$ approaches 0, this ratio approaches 1.

Now assume that the distance between the propeller streamtube and the shear layer of the potential core remains fixed as the fluid passes by the propeller. This distance is given by

$$\Delta r = \frac{d_j}{2} - r_s \tag{B6}$$

where

$$r_s = \frac{A_s}{\pi} \tag{B7}$$

and $A_s$ is given by equation (B5).

Thus, the radius of the potential core at the disk plane is given by

$$r_o = \frac{d_p}{2} + r_s \tag{B8}$$

and it is this predicted value that appears in figures 9 and 10 and in table II.

For the present experiment and for future tests in the QFF, equation (B5) can also be used in the following way. First, it can be rewritten

$$\frac{d_s^2}{d_p^2 - d_{body}^2} = \frac{1}{2}\left[1 + \sqrt{1 + \frac{8d_p^2 C_T}{\pi(d_p^2 - d_{body}^2)J^2}}\right] \tag{B9}$$

where $d_s$ represents the diameter of the streamtube at the jet exit that contracts to the diameter of the propeller at the disk plane. For the QFF, $d_s$ must be less than $d_j$ = 1.22 m (4 ft). However, there are two other factors to consider. By the

action of viscosity, the potential core is reduced to 88 percent of its exit diameter by the time the flow reaches the plane of the disk. Furthermore, to eliminate the need for empirical correction factors, reference 1 recommends a margin of about 30 percent of $d_j$ between the propeller tip and the shear layer. Thus,

$$d_s < (0.88)(0.70)d_j \tag{B10}$$

With this guideline and the relationship of propeller thrust in producing contraction (eq. (B9)), we can establish bounds on propeller performance for which meaningful aerodynamic data can be obtained:

$$\frac{(0.62d_j)^2}{d_p^2 - d_{body}^2} > \frac{1}{2}\left[1 + \sqrt{1 + \frac{8d_p^2 C_T}{\pi(d_p^2 - d_{body}^2)J^2}}\right] \tag{B11}$$

From this relationship, we obtain

$$\frac{C_T}{J^2} < \frac{\pi}{8}\left(\frac{d_p^2 - d_{body}^2}{d_p^2}\right)\left\{\left[\frac{2(0.62d_j)^2}{d_p^2 - d_{body}^2} - 1\right]^2 - 1\right\} \tag{B12}$$

For the propeller tested on the PTS in the QFF, this relationship becomes

$$\frac{C_T}{J^2} < 0.633 \tag{B13}$$

Data that did not meet this criterion were purged from the data base.

## APPENDIX C

### DISCUSSION OF DATA PURGE DUE TO MECHANICAL FRICTION

Since the thrust tares varied unpredictably yet persistently during the test program, it is necessary to analyze and bound the uncertainties in the thrust data. The thrust coefficient is calculated via

$$C_T = \frac{T}{\rho n^2 d_p^4} = \frac{T_{meas} - T_{tares}}{\rho n^2 d_p^4}$$

The change in $C_T$ caused by an error in the offset may be estimated in the following way:

$$\frac{\delta C_T}{\delta(\text{Offset})} = -\frac{1}{\rho n^2 d_p^4}$$

Since the density $\rho$ and the diameter $d_p$ are fixed, the error in $C_T$ caused by the error in the offset depends only on the motor rps setting $n$; that is,

$$|\Delta C_T| = \left|\frac{\Delta(\text{Offset})}{\rho n^2 d_p^4}\right|$$

The offset error is arbitrarily set at 4.4 N (1 lb). This is a maximum value and was chosen based on the behavior of the PTS during a single run of the experiment. The maximum tolerable error in $C_T$ is chosen to be 5 percent of the full-scale ordinate value on the plots (e.g., if $(C_T)_{\text{full-scale}} = 0.15$, then $\Delta C_T = 0.008$). Data were thus purged when

$$\left|\frac{\Delta(\text{Offset})}{\rho n^2 d_p^4}\right| > |\Delta C_T|$$

or when

$$n < \sqrt{\frac{|\Delta(\text{Offset})|}{\rho d_p^4 |\Delta C_T|}} \qquad \text{(C1)}$$

In this way the uncertainties in $C_T$ caused by the mechanical design problems are limited to less than 0.004 for a blade pitch angle of 5° and less than 0.008 for a blade pitch angle of 17°.

## REFERENCES


1. Glauert, H.: Airplane Propellers. Volume IV of Aerodynamic Theory, div. L, W. F. Durand, ed., Julius Springer (Berlin), 1935, pp. 169-360.

2. Bocci, A. J.: A New Series of Aerofoil Sections Suitable for Aircraft Propellers. Aeronaut. Q., vol. 28, pt. 1, Feb. 1977, pp. 59-73.

3. Korkan, Kenneth D.; Gregorek, Gerald M.; and Mikkelsen, Daniel C.: A Theoretical and Experimental Investigation of Propeller Performance Methodologies. AIAA-80-1240, June-July 1980.

4. Farassat, F.; and Succi, G. P.: A Review of Propeller Discrete Frequency Noise Prediction Technology With Emphasis on Two Current Methods for Time Domain Calculations. J. Sound & Vib., vol. 71, no. 3, Aug. 8, 1980, pp. 399-419.

5. Goldstein, Sydney: On the Vortex Theory of Screw Propellers. Proc. R. Soc. London, ser. A, vol. 123, no. 791, Mar. 6, 1929, pp. 440-465.

6. Lock, C. N. H.: The Application of Goldstein's Theory to the Practical Design of Airscrews. R. & M. No. 1377, British A.R.C., 1932.

7. Cox, R. A.: Low Speed, Flat Plate, Carborundum Grit Trip Strip. AIAA-80-0868, May 1980.

8. Taylor, John W. R., ed.: Jane's All the World's Aircraft 1977-78. Jane's Yearbooks (London).

TABLE I.- TEST CONDITIONS

| Runs | Propeller | Grit | Pitch angle | Nominal velocities, m/s (ft/s) | Purpose |
|---|---|---|---|---|---|
| 1-18 | Off | | | 19.5, 30, 36.6 (64, 98, 120) | Potential core surveys |
| 34-36 | Off | | | 12, 18, 24 (40, 60, 80) | Potential core surveys |
| 40-42 | Off | | | 18, 27, 36.6 (60, 90, 120) | Potential core surveys |
| 20-28 | On | None | 5° | 12, 18, 27 (40, 60, 90) | Check repeatability |
| 66-60 | On | Both sides | 17° | 18, 27, 36.6 (60, 90, 120) | Check repeatability |
| 28-33 | On | None | 5° | 12, 18, 24 (40, 60, 80) | Measure aerodynamic performance and potential core position |
| 46-48 | On | Suction side | 5° | 12, 18, 24 (40, 60, 80) | Measure aerodynamic performance and potential core position |
| 52-54 | On | Both sides | 5° | 12, 18, 24 (40, 60, 80) | Measure aerodynamic performance and potential core position |
| 37-39 43-45 | On | None | 17° | 18, 27, 36.6 (60, 90, 120) | Measure aerodynamic performance and potential core position |
| 49-51 | On | Suction side | 17° | 18, 27, 36.6 (60, 90, 120) | Measure aerodynamic performance and potential core position |
| 55-57 | On | Both sides | 17° | 18, 27, 36.6 (60, 90, 120) | Measure aerodynamic performance and potential core position |

TABLE II.- MEASURED AND PREDICTED POSITIONS OF THE POTENTIAL CORE KNEE

| Pitch angle | $U_j$, m/s (ft/s) | rpm | J | $C_T/J^2$ | Position, $r_o/d_j$ | | Error, percent |
|---|---|---|---|---|---|---|---|
| | | | | | Measured | Predicted | |
| 5° | 12 (40) | 3006 | 0.361 | 0.11 | 0.44 | 0.44 | 0 |
| | | 5005 | .218 | .95 | .43 | .40 | 7 |
| | | 7000 | .158 | 2.32 | .41 | .36 | 12.2 |
| | 18 (60) | 4006 | .403 | .04 | .45 | .45 | 0 |
| | | 6006 | .269 | .51 | .44 | .42 | 4.5 |
| | | 7501 | .217 | 1.04 | .42 | .39 | 7.1 |
| | 24 (80) | 6007 | .357 | .16 | .45 | .44 | 2.2 |
| | | 7927 | .271 | .55 | .43 | .42 | 2.3 |
| | | | | | | Average ..... | 4.4 |
| 17° | 18 (60) | 2005 | 0.80 | 0.04 | 0.46 | 0.45 | 2.2 |
| | | 4000 | .399 | .64 | .43 | .41 | 4.7 |
| | 27 (90) | 3499 | .686 | .13 | .45 | .44 | 2.2 |
| | | 4500 | .533 | .31 | .45 | .43 | 4.4 |
| | | 5500 | .437 | .54 | .43 | .42 | 2.3 |
| | 36.6 (120) | 4000 | .795 | .08 | .45 | .45 | 0 |
| | | 6000 | .528 | .33 | .45 | .43 | 4.4 |
| | | 7400 | .432 | .60 | .41 | .41 | 0 |
| | | | | | | Average ..... | 2.5 |

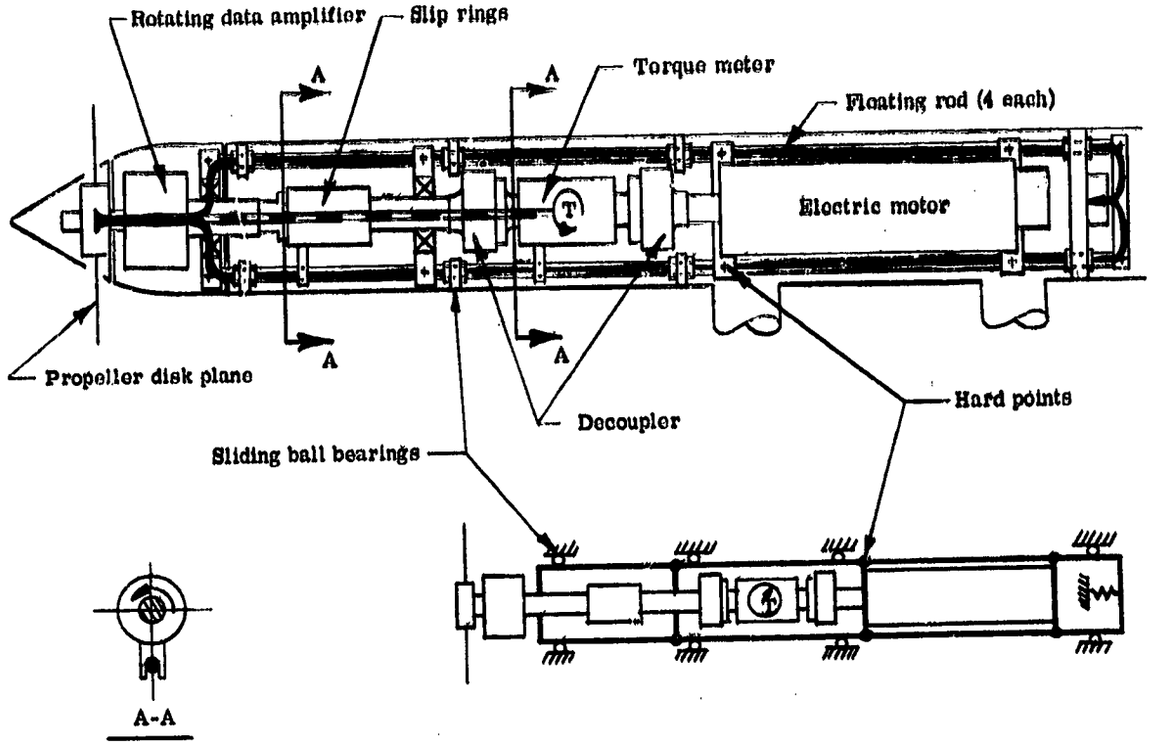


Figure 1.- Diagram of the components in the centerbody of the propeller test stand (PTS).

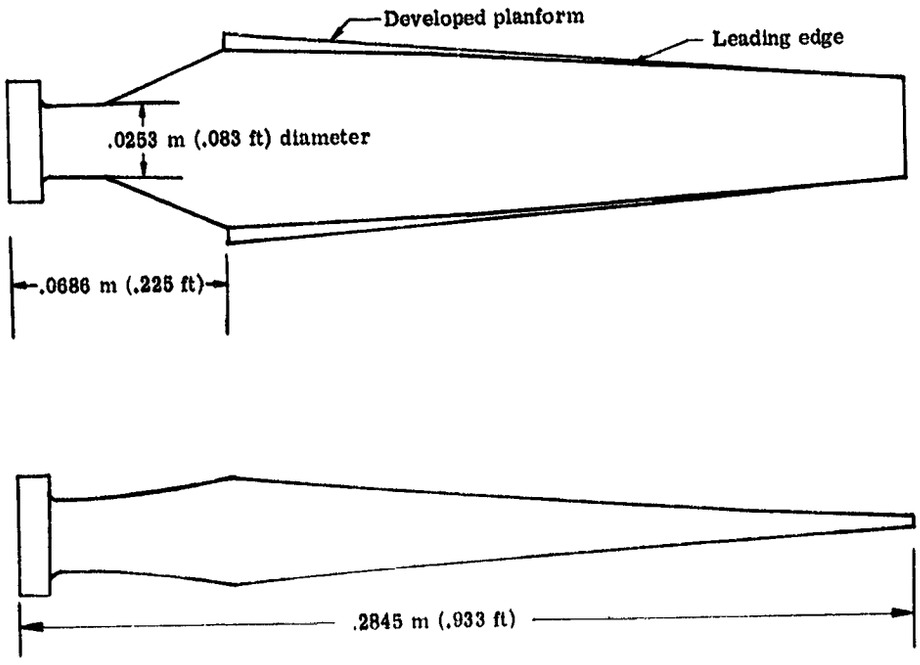


Figure 2.- Propeller used during the PTS evaluation.

ORIGINAL PAGE
BLACK AND WHITE PHOTOGRAPH

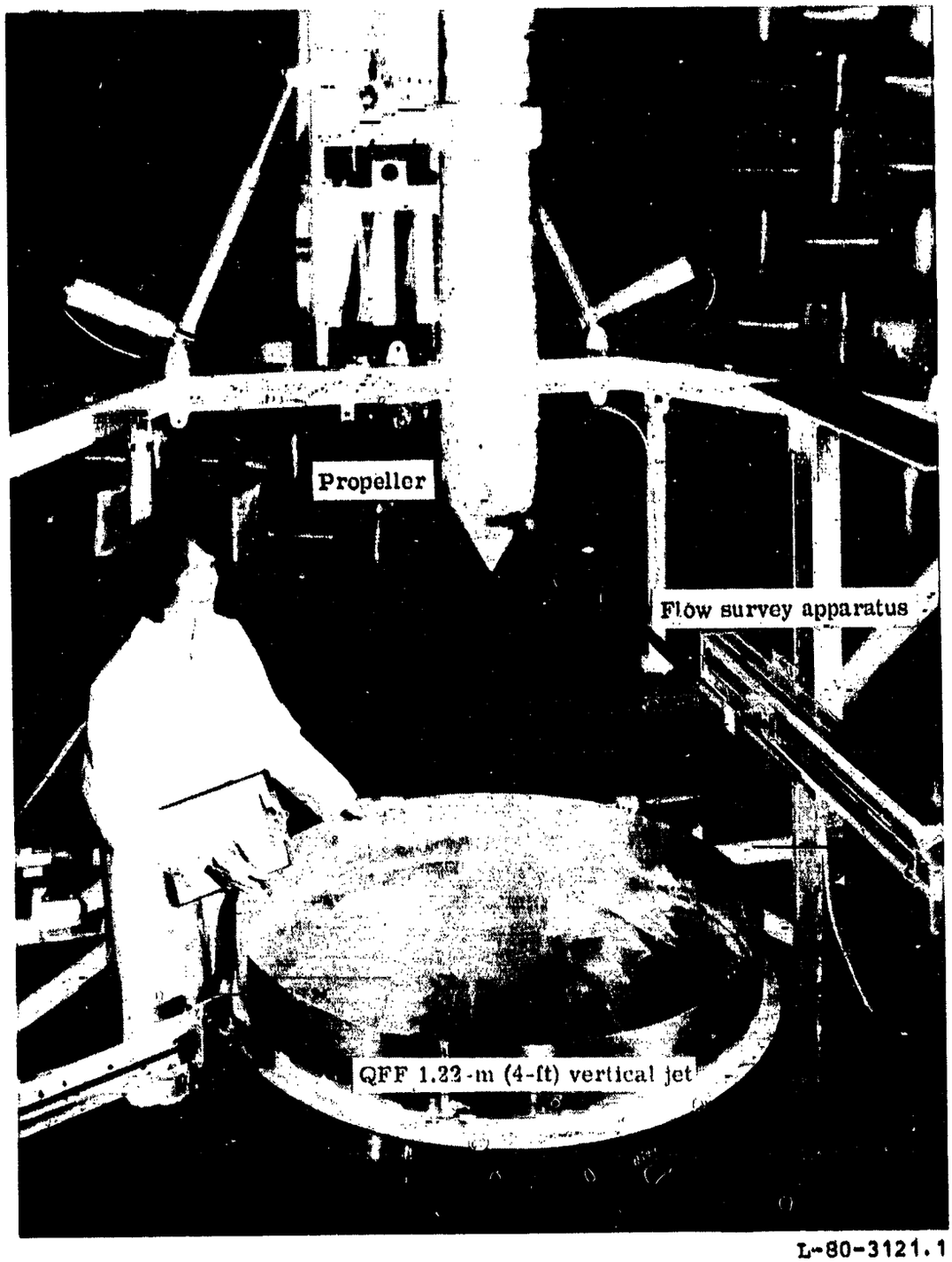


L-80-3121.1

Figure 3.- Experimental setup in ANRL.

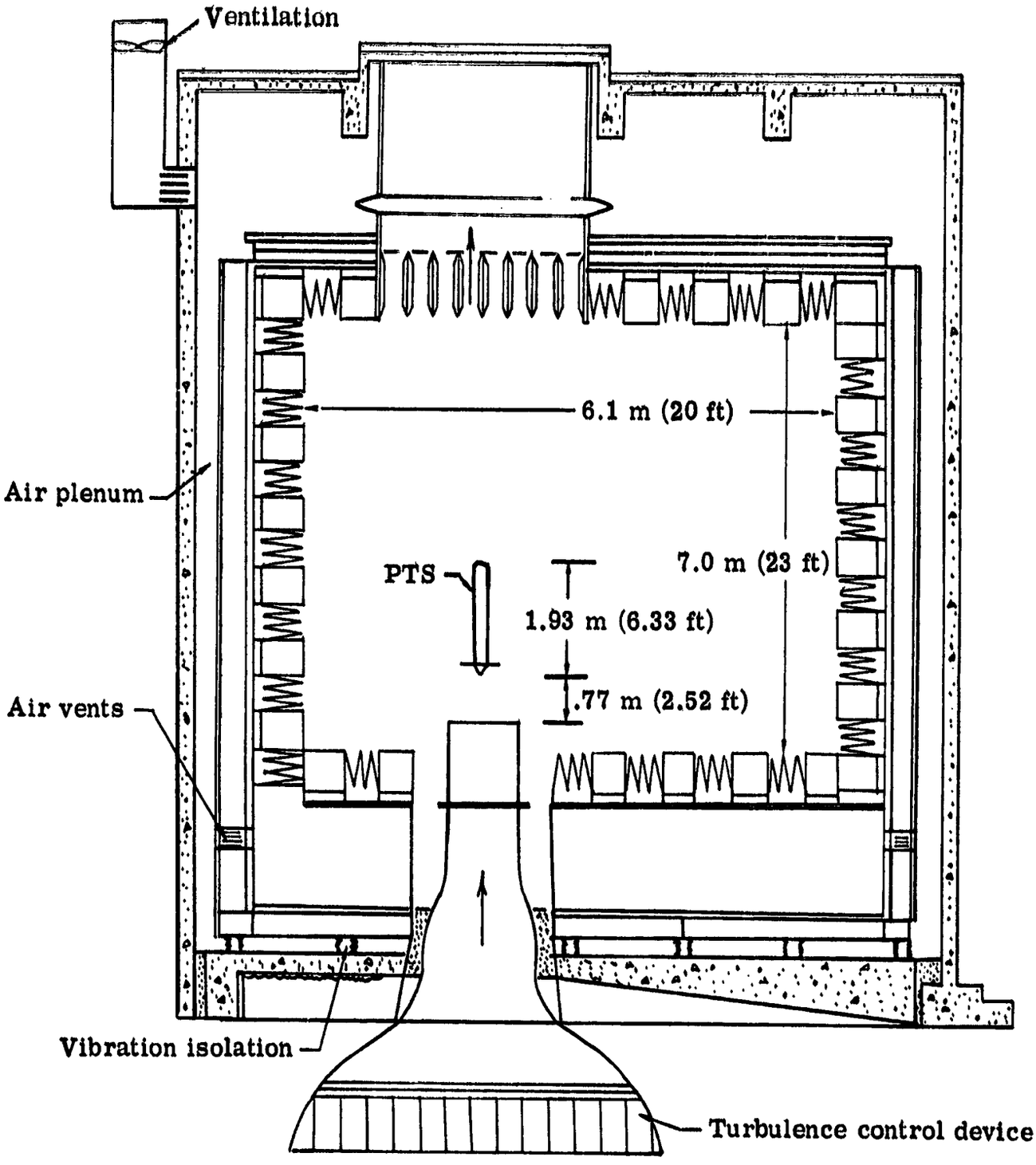


Figure 4.- Sketch of the QFF with the PTS installed.

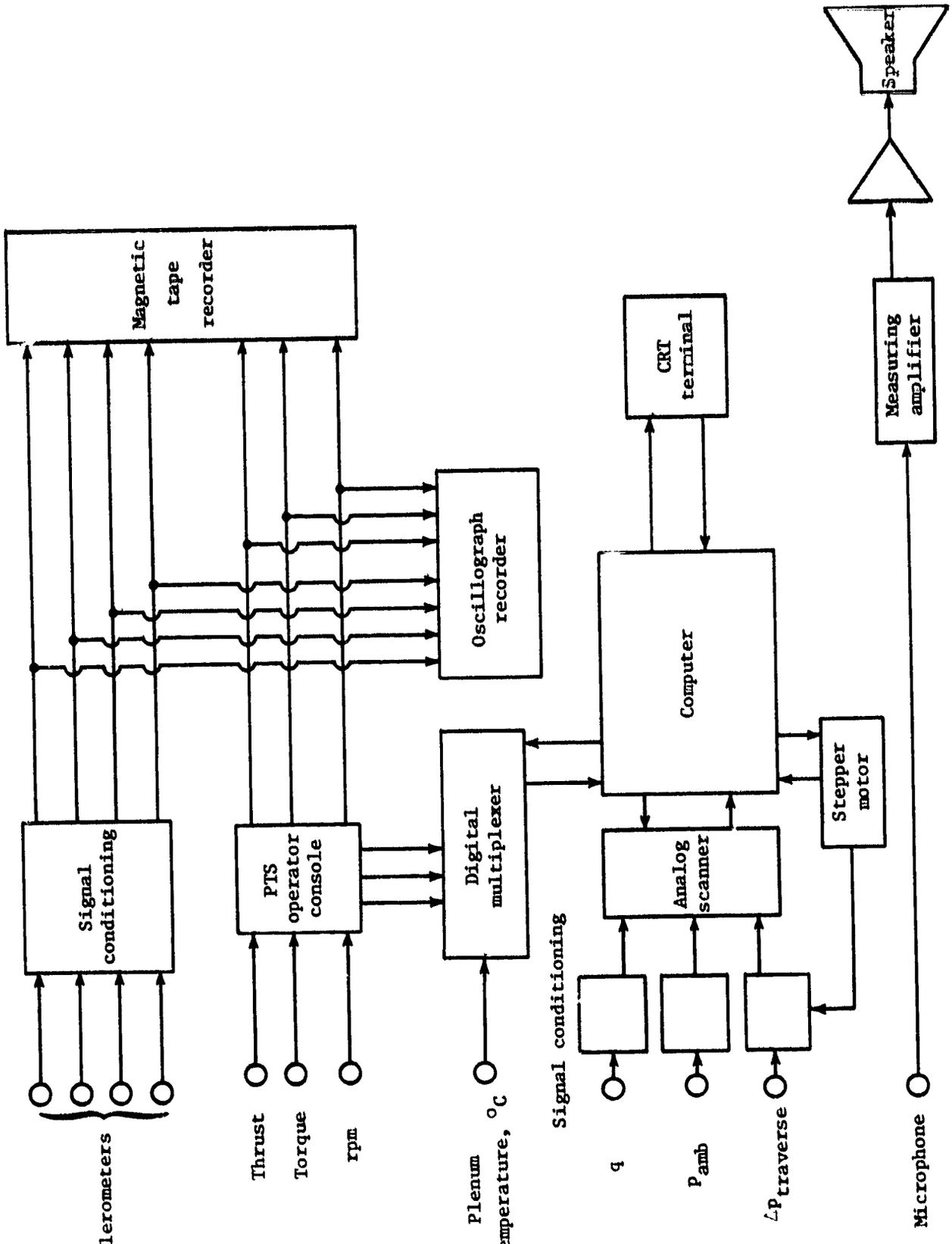


Figure 5.- Instrumentation diagram.

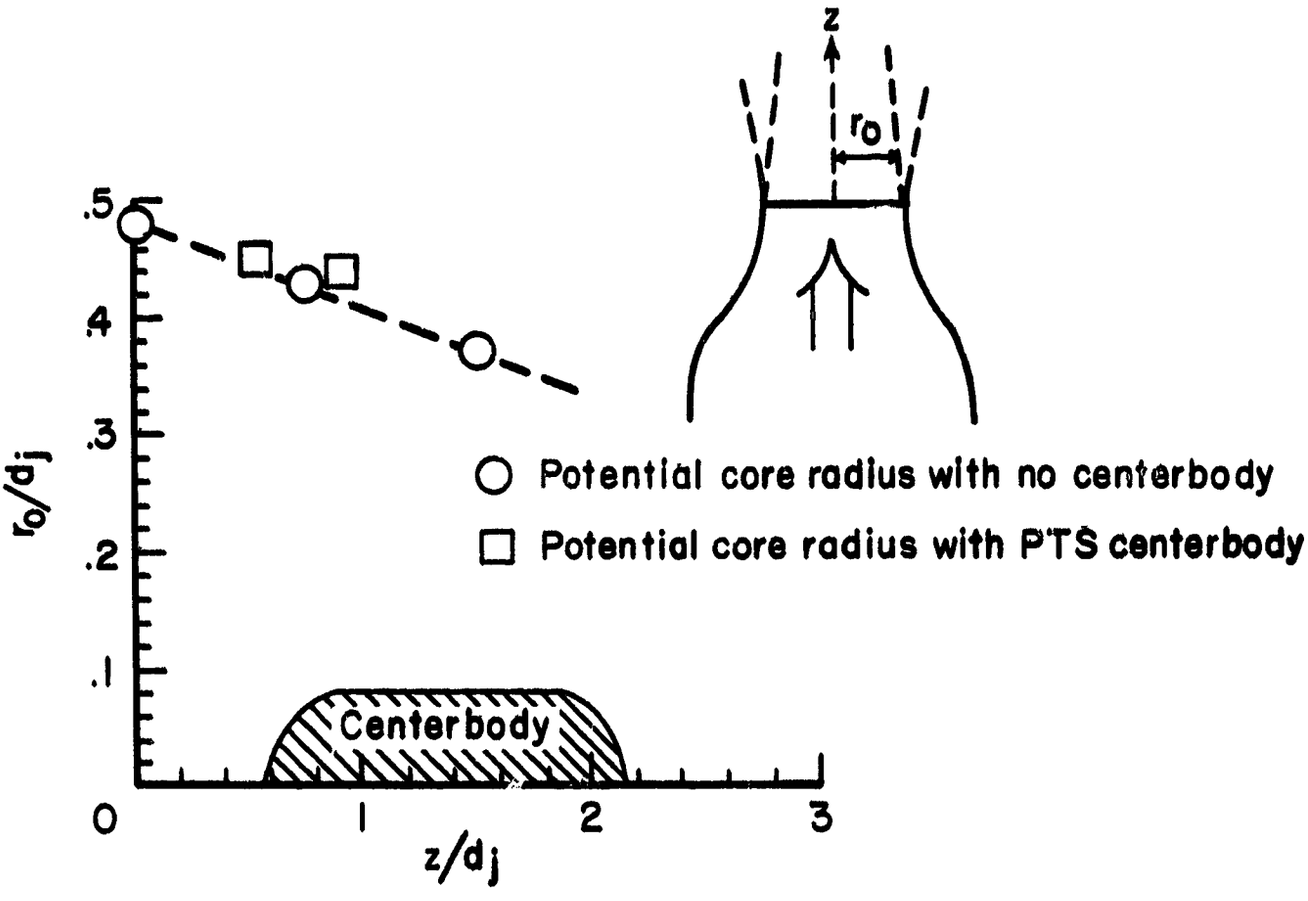


Figure 6.- Effect of the centerbody on the extent of the potential core region. U = 30 m/s (98.4 ft/s).

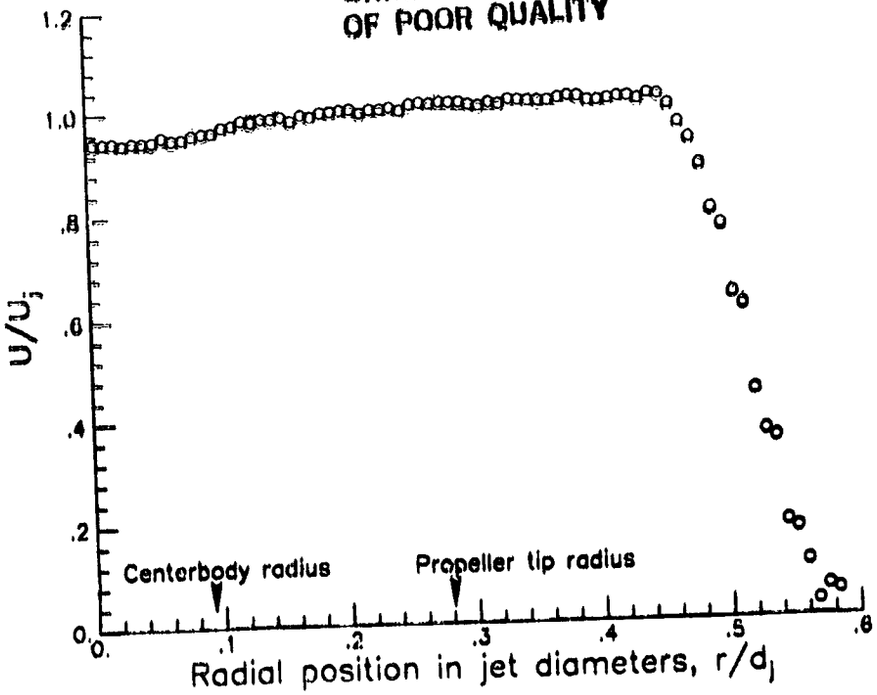


Figure 7.- Representative velocity profile 0.15 m (6 in.) upstream of propeller disk location.

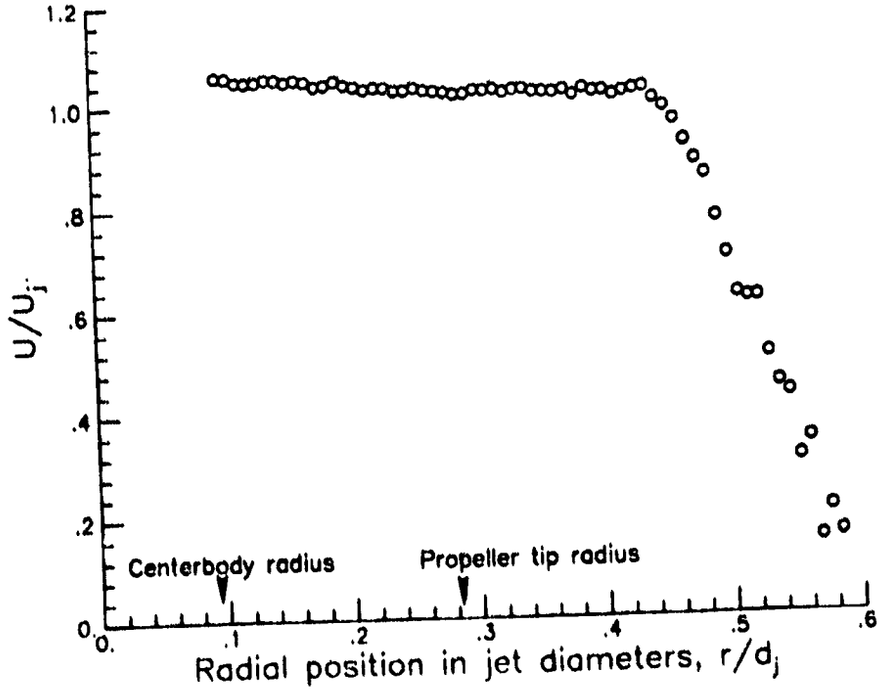


Figure 8.- Representative velocity profile 0.15 m (6 in.) downstream of propeller disk location.

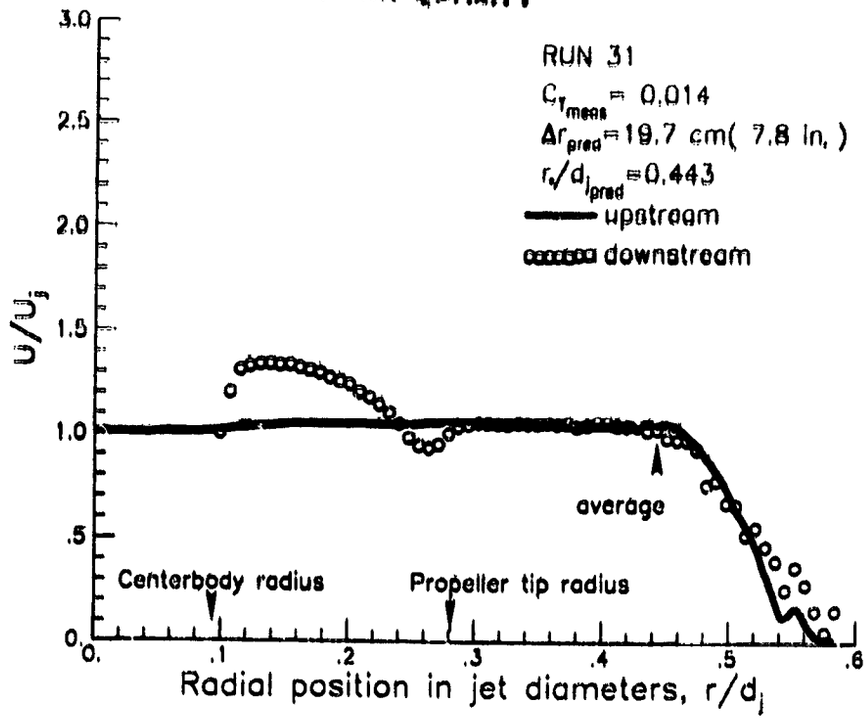


(a) $U_j$ = 12 m/s (40 ft/s); 3000 rpm.

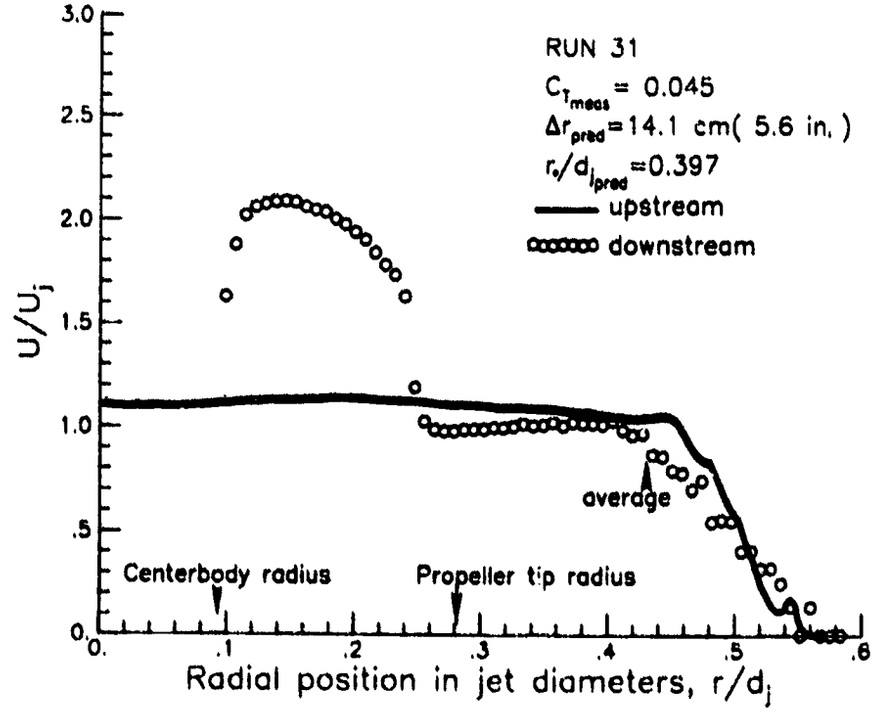


(b) $U_j$ = 12 m/s (40 ft/s); 5000 rpm.

Figure 9.- Potential core surveys for blade pitch angle of 5°.

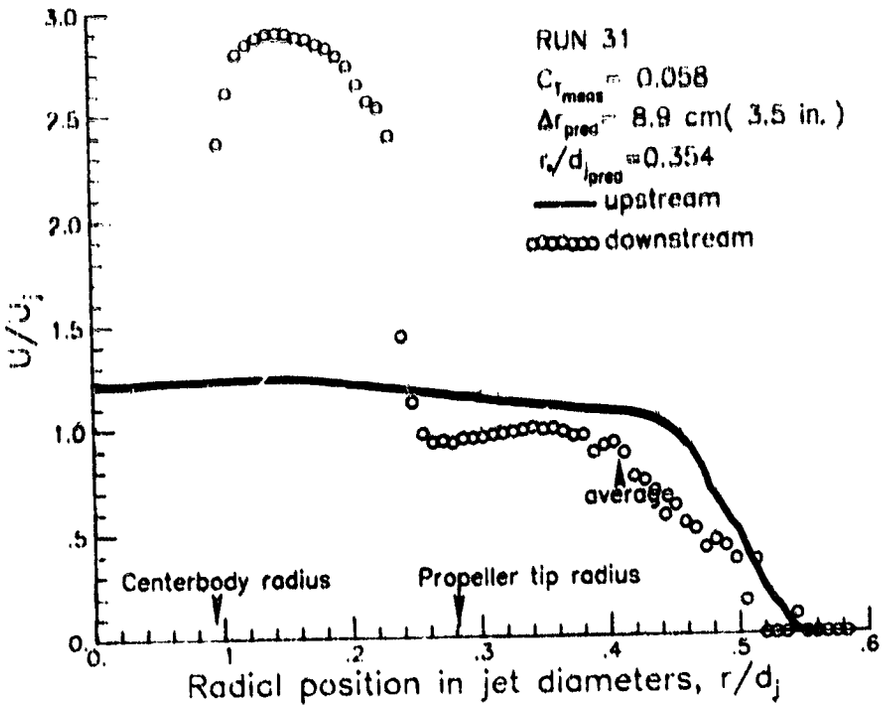


(c) $U_j$ = 12 m/s (40 ft/s); 7000 rpm.

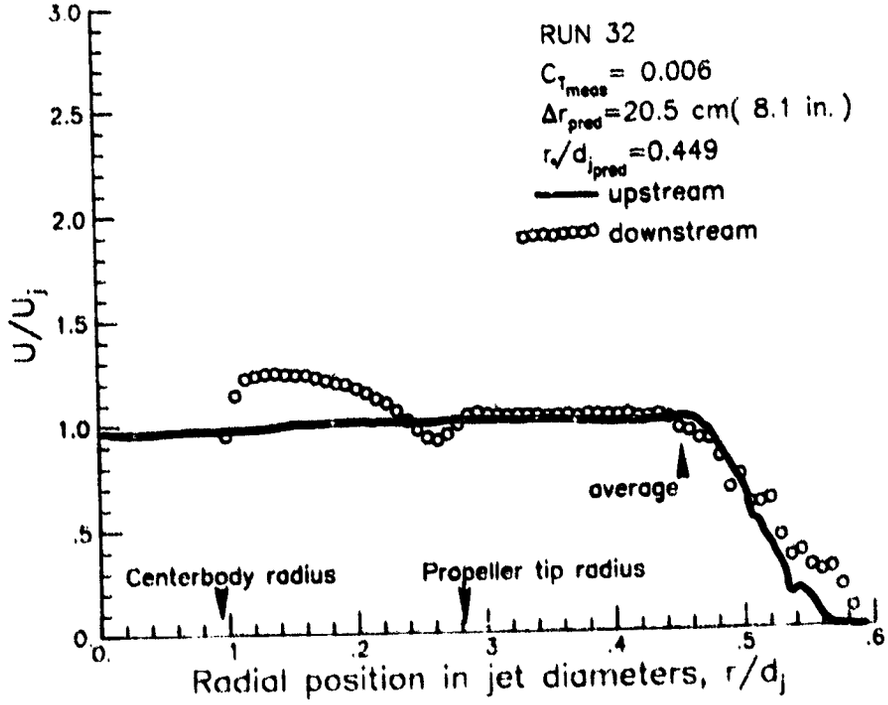


(d) $U_j$ = 18 m/s (60 ft/s); 4000 rpm.

Figure 9.- Continued.

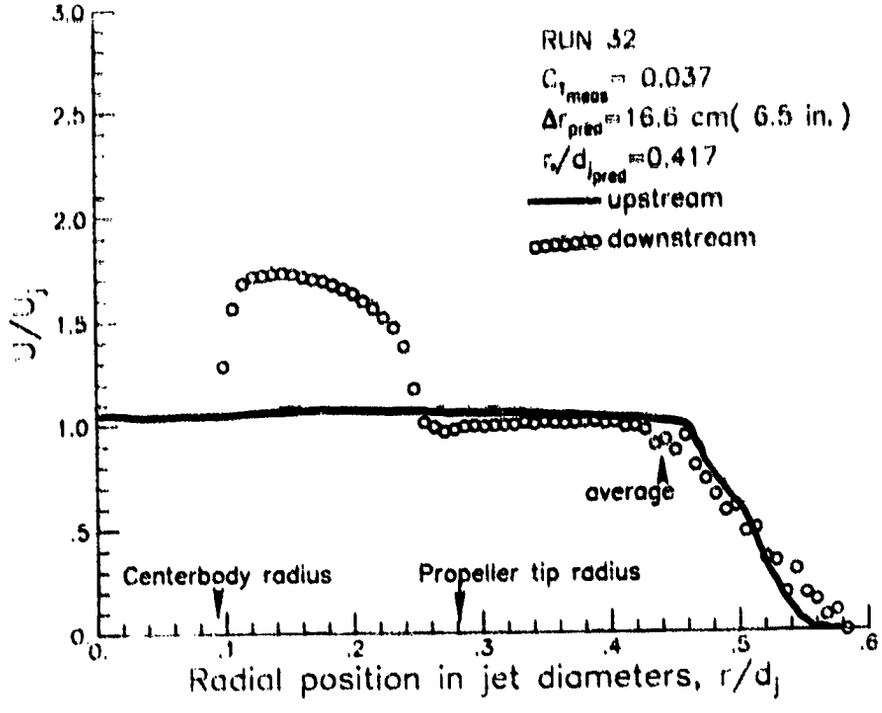


(e) $U_j$ = 18 m/s (60 ft/s); 6000 rpm.

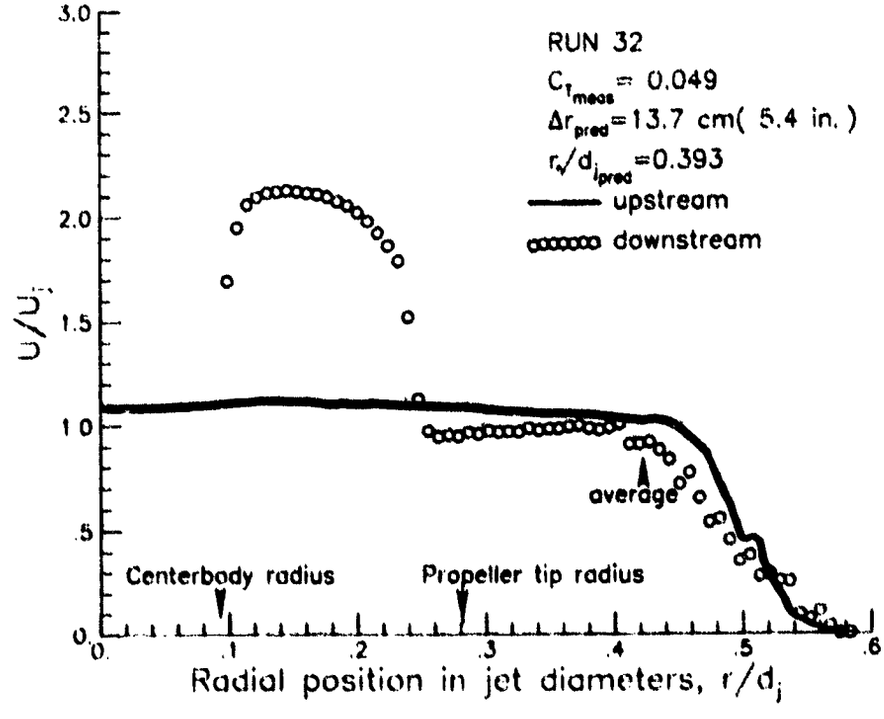


(f) $U_j$ = 18 m/s (60 ft/s); 7500 rpm.

Figure 9.- Continued.

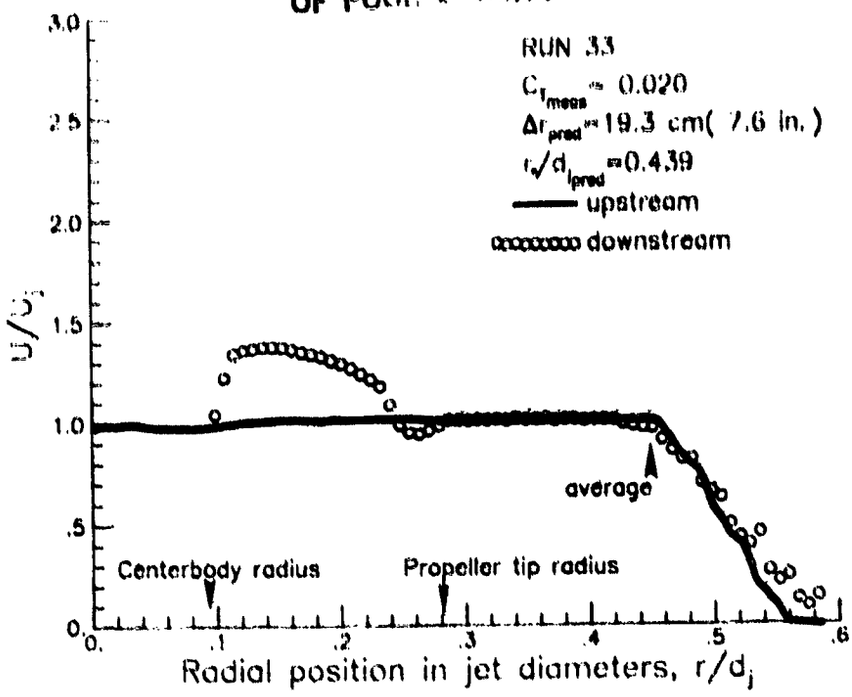


(g) $U_j$ = 24 m/s (80 ft/s); 6000 rpm.

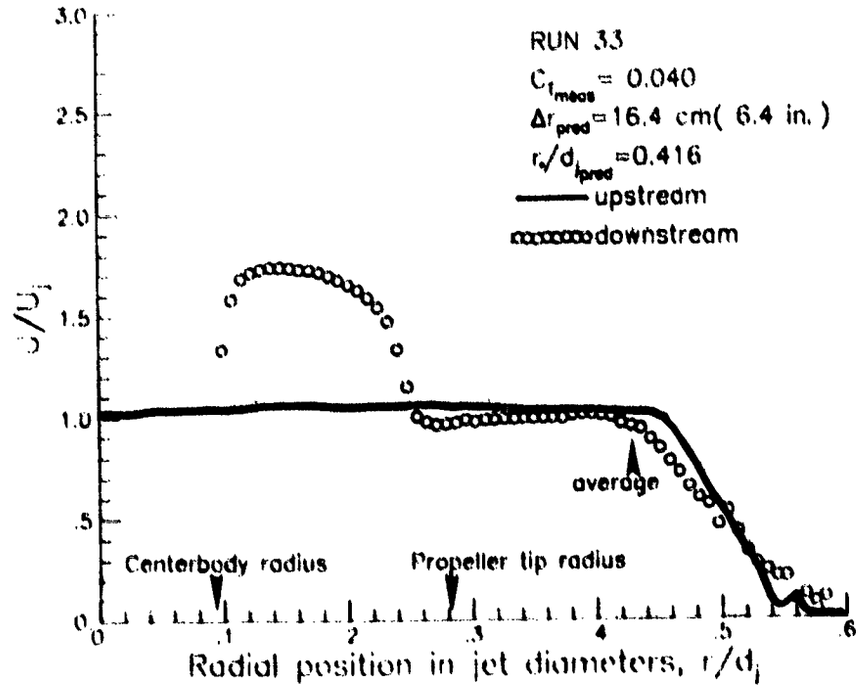


(h) $U_j$ = 24 m/s (80 ft/s); 8000 rpm.

Figure 9.- Concluded.

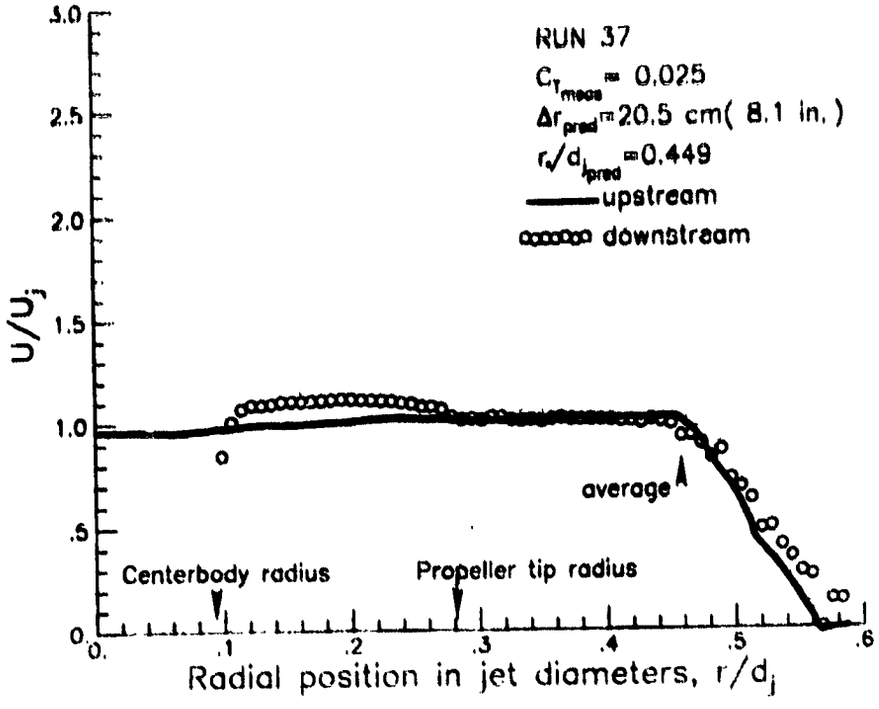


(a) $U_j$ = 18 m/s (60 ft/s); 2000 rpm.

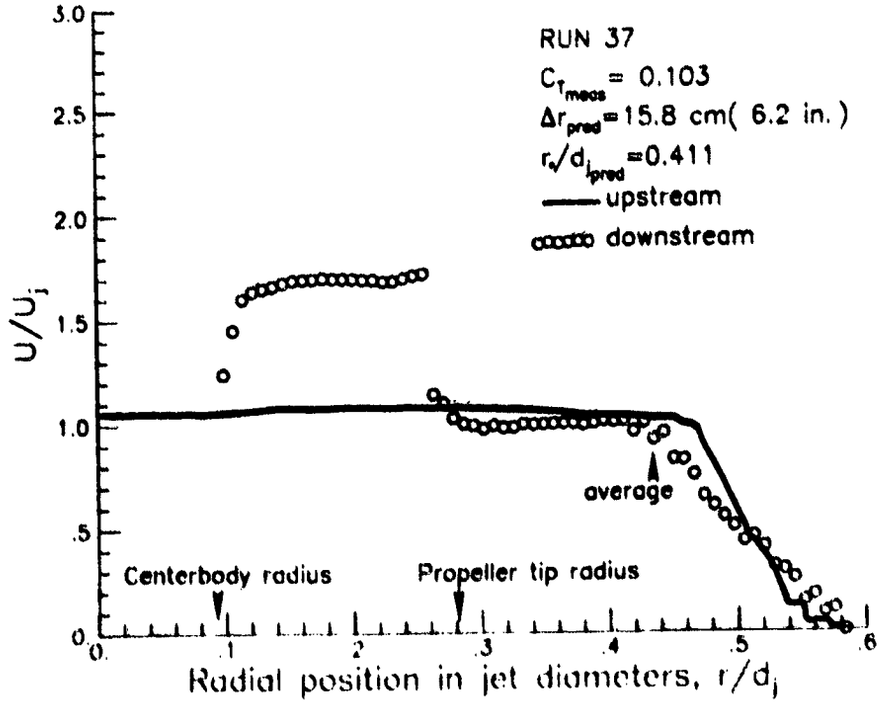


(b) $U_j$ = 18 m/s (60 ft/s); 4000 rpm.

Figure 10.- Potential core surveys for blade pitch angle of 17°.

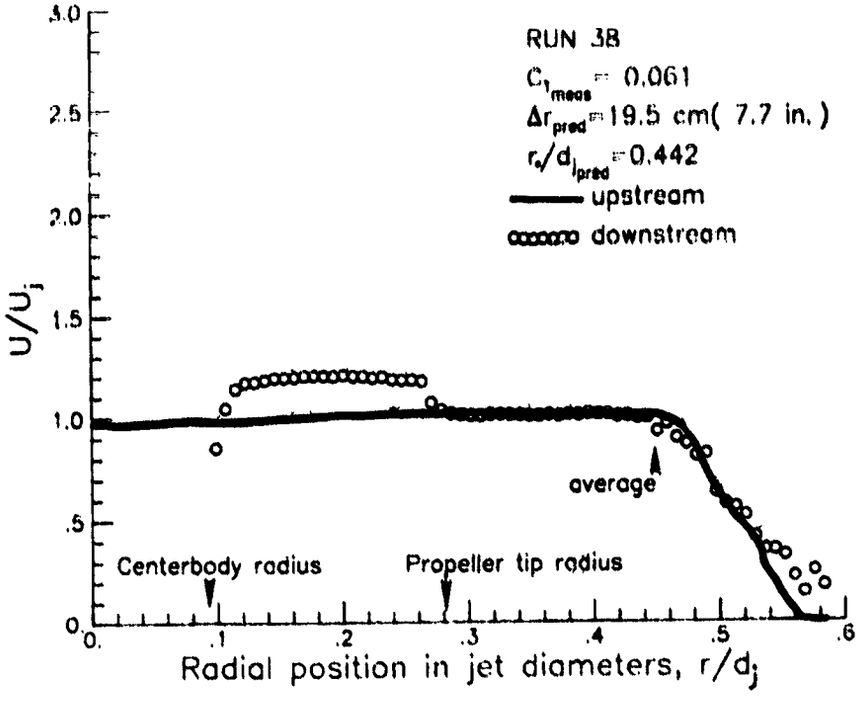


(c) $U_j$ = 27 m/s (90 ft/s); 3500 rpm.

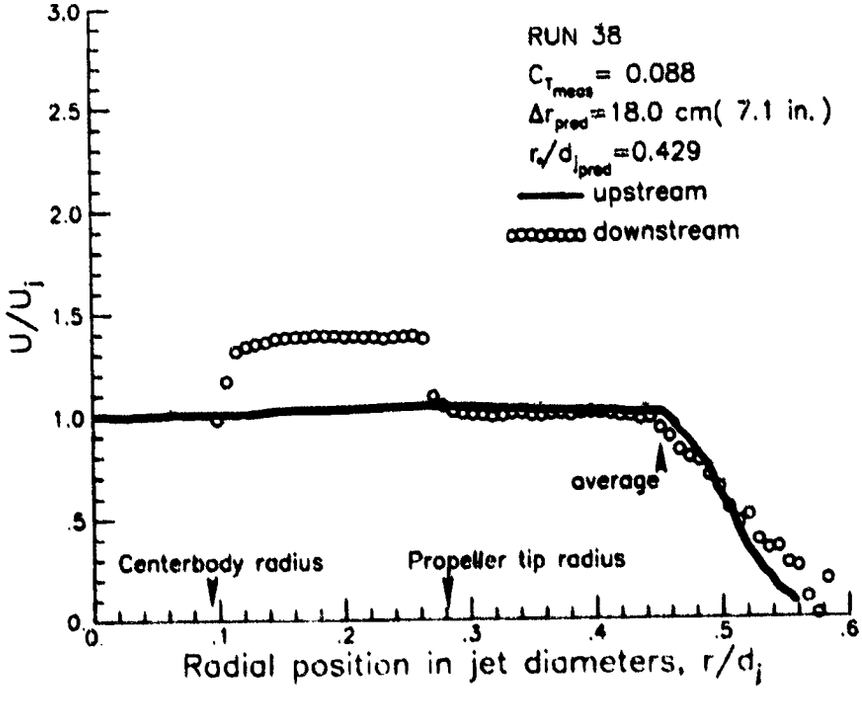


(d) $U_j$ = 27 m/s (90 ft/s); 4500 rpm.

Figure 10.- Continued.

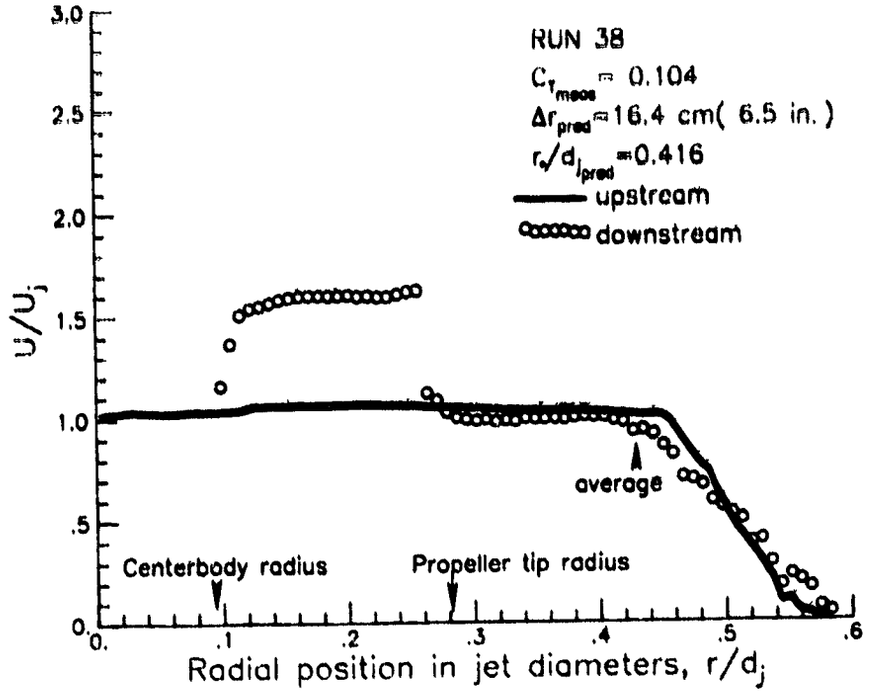


(e) $U_j$ = 27 m/s (90 ft/s); 5500 rpm.

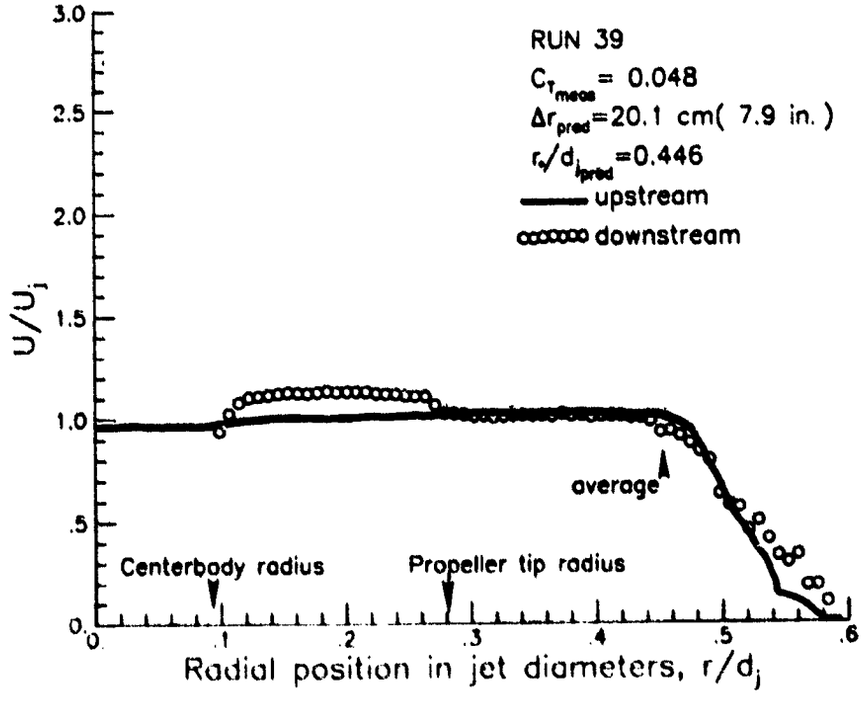


(f) $U_j$ = 36.6 m/s (120 ft/s); 4000 rpm.

Figure 10.- Continued.

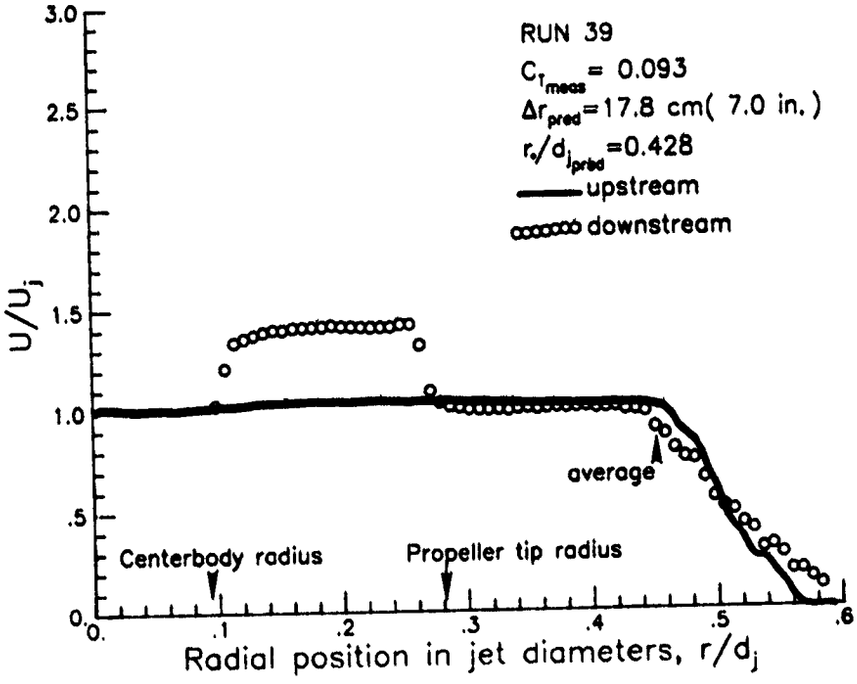


(g) $U_j$ = 36.6 m/s (120 ft/s); 6000 rpm.

Figure 10.- Concluded.

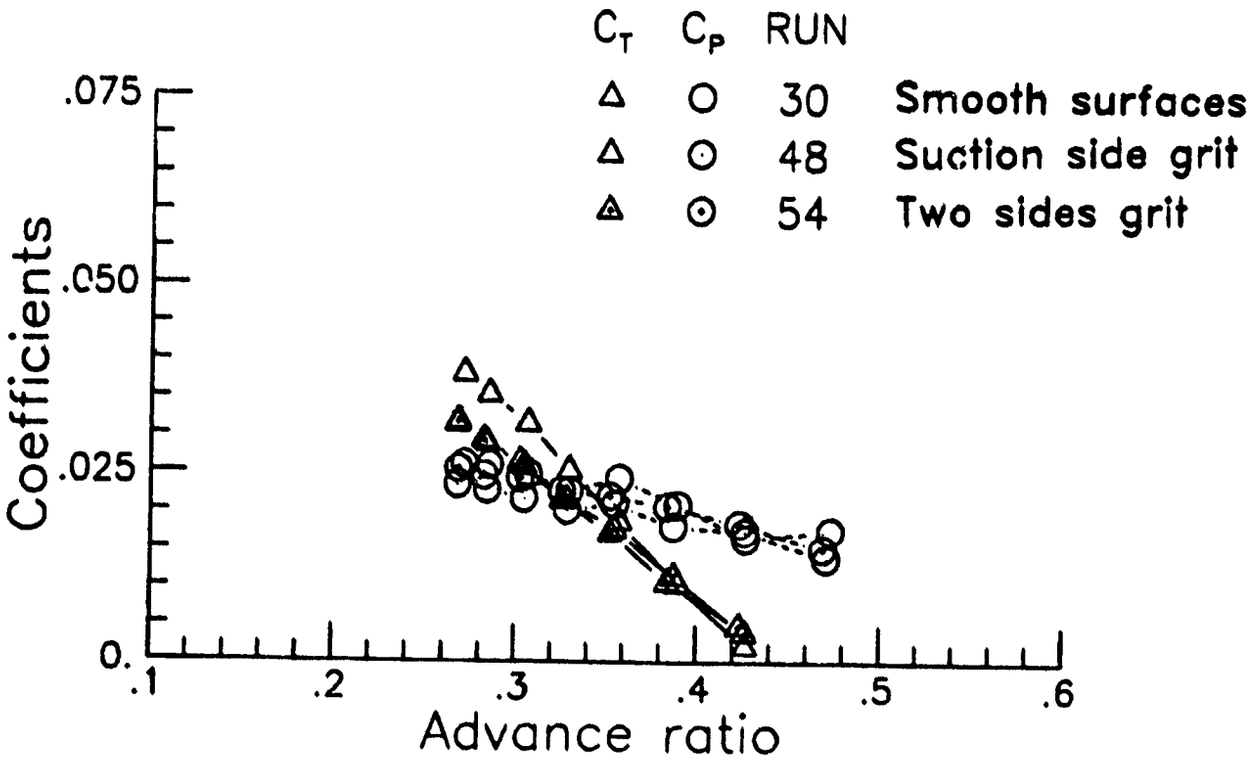


Figure 11.- Effect on aerodynamic performance of adding grit to blade with 5° of pitch. $U_j$ = 24 m/s (80 ft/s).

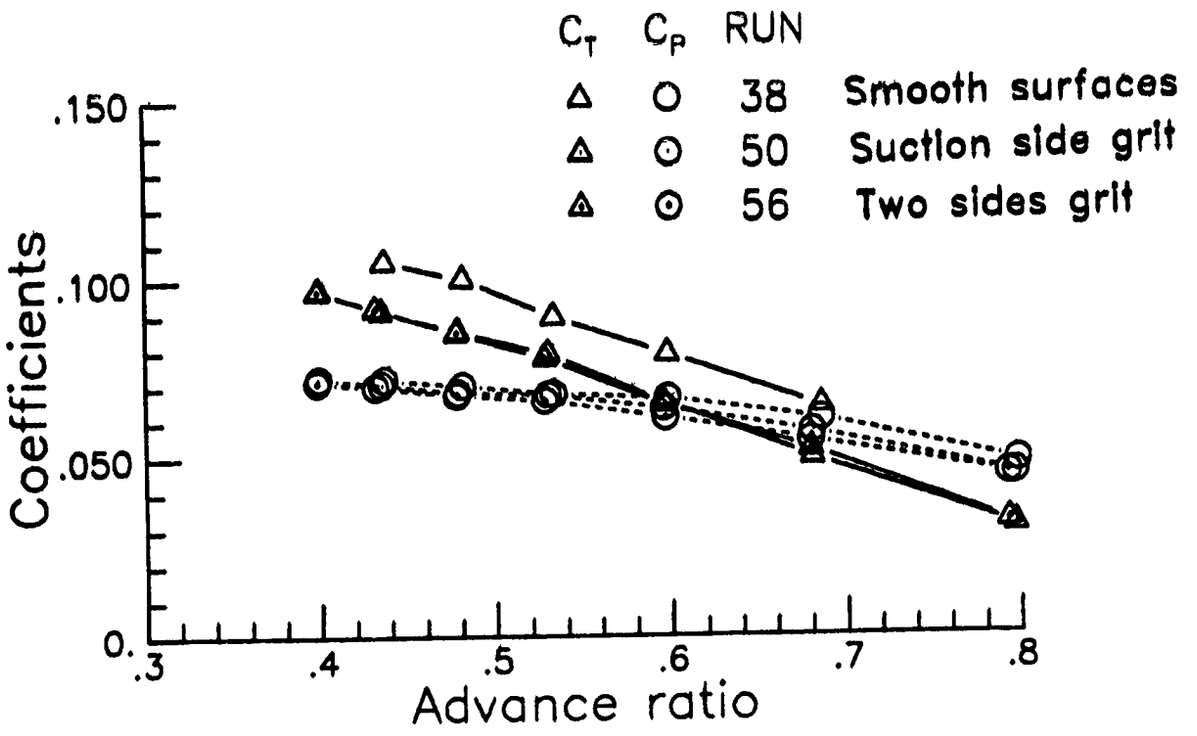


(a) $U_j$ = 27 m/s (90 ft/s).

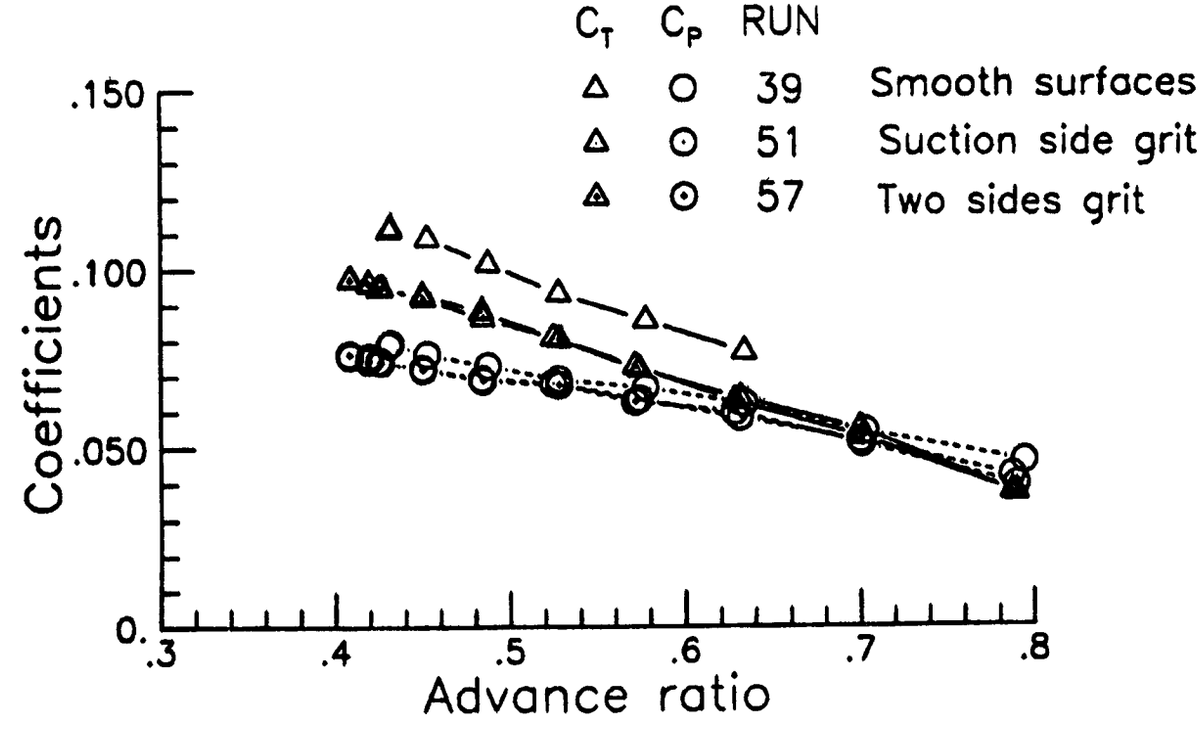


(b) $U_j$ = 36.6 m/s (120 ft/s).

Figure 12.- Effect on aerodynamic performance of adding grit to blade with 17° of pitch.

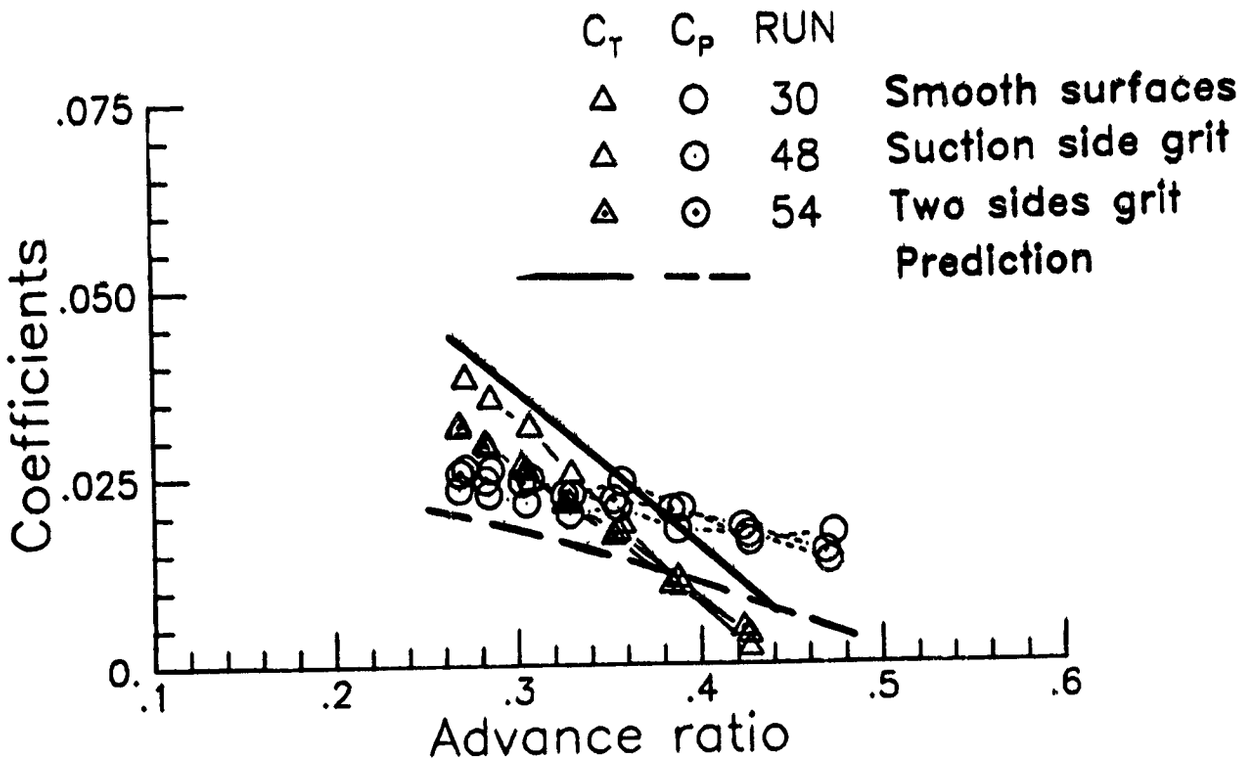


Figure 13.- Measured and predicted aerodynamic performance for blade pitch angle of 5°. $U_j$ = 24 m/s (80 ft/s).

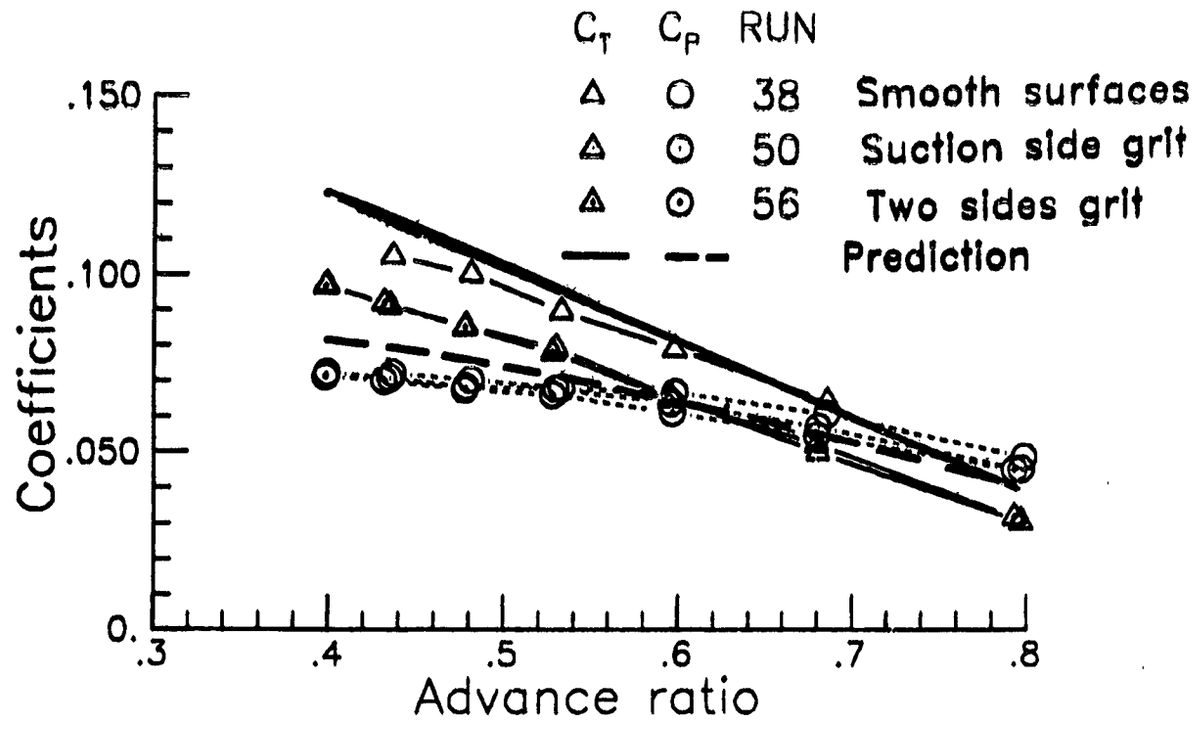


(a) $U_j$ = 27 m/s (90 ft/s).

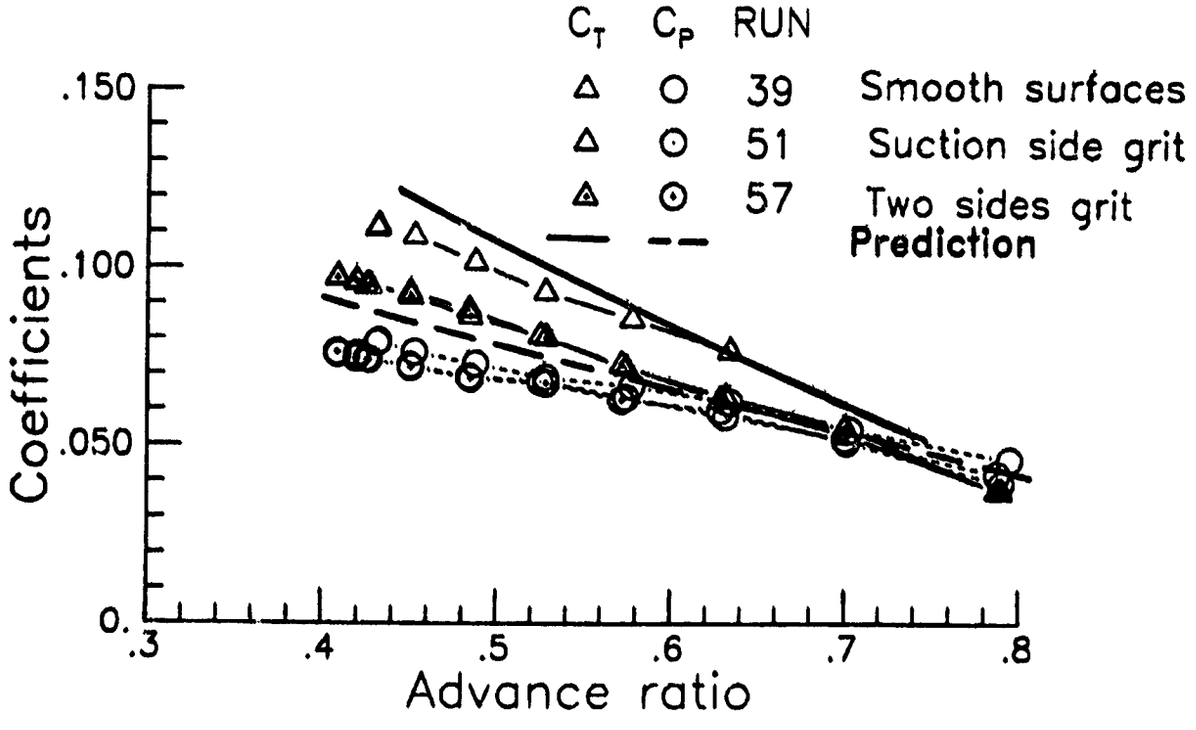


(b) $U_j$ = 36.6 m/s (120 ft/s).

Figure 14.- Measured and predicted aerodynamic performance for blade pitch angle of 17°.

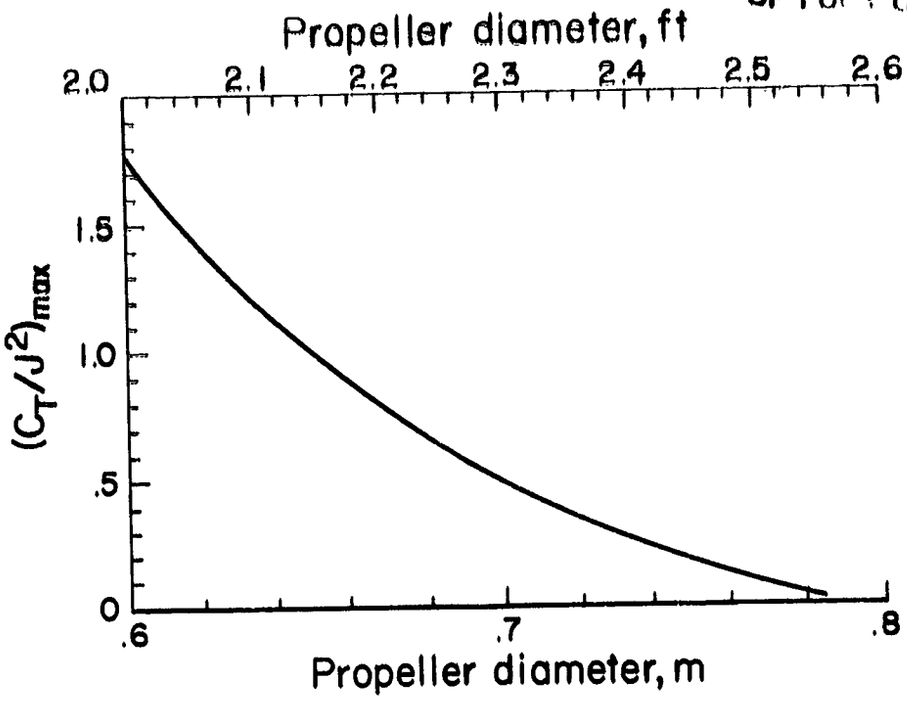


Figure 15.- Propeller operational limitation for the PTS in the QFF.

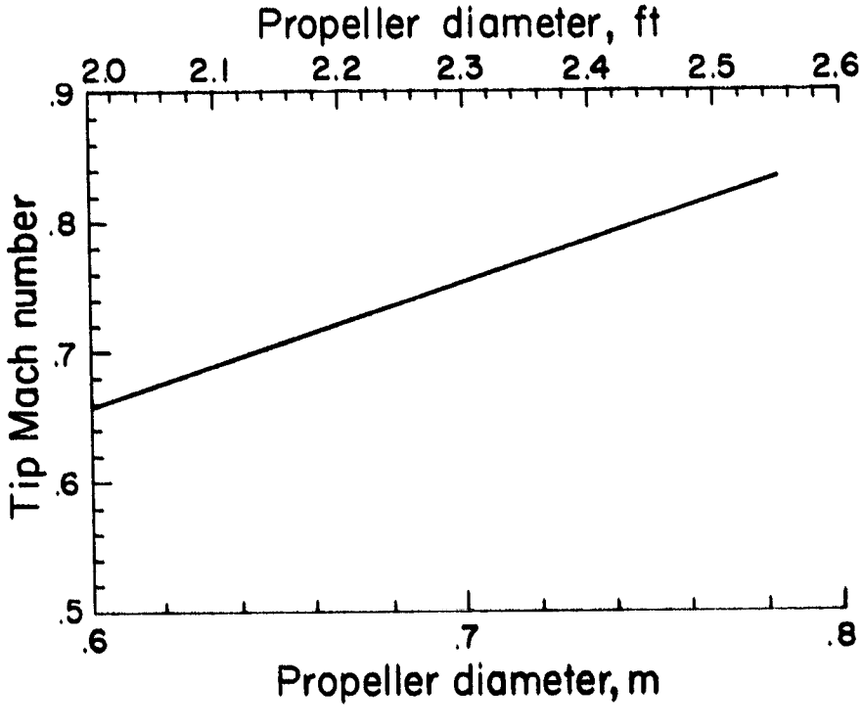


Figure 16.- Maximum tip Mach number attainable with the PTS.
$U_j$ = 36.6 m/s (120 ft/s); 7000 rpm.

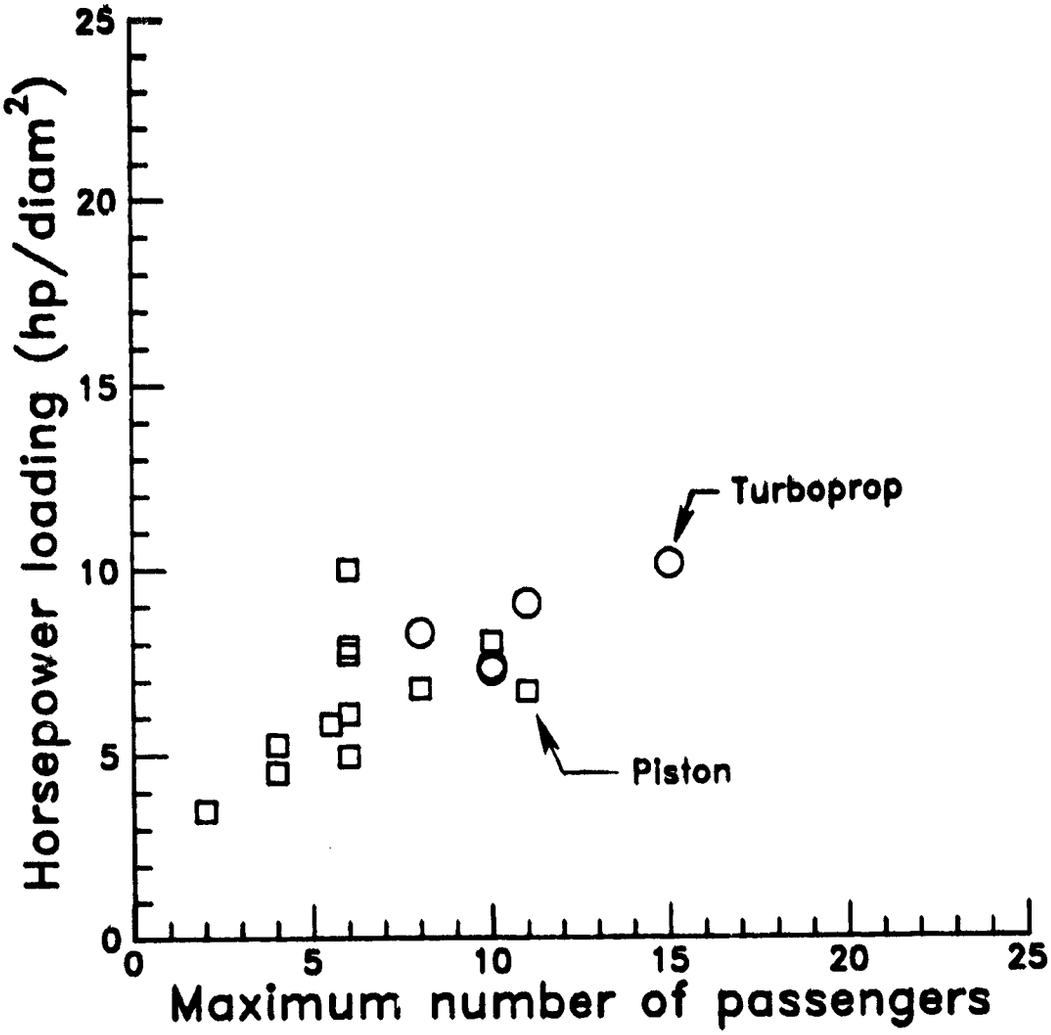


Figure 17.- Propeller power loading for a sample of general aviation aircraft.